https://doi.org/10.5194/egusphere-2026-554
Preprint. Discussion started: 11 February 2026

Impacts of mesoscale atmospheric subsidence on cloud glaciation and decoupling in Arctic marine cold air outbreaks

Fiona Paulus[1], Joshua J. Müller[2], Benjamin Kirbus[2,3], Harald Sodemann[4,5], Lars van Gelder[1], Andreas Walbröl[1], Manfred Wendisch[2], and Roel A. J. Neggers[1]

[1]University of Cologne, Institute for Geophysics and Meteorology, Cologne, Germany
[2]University Leipzig, Leipzig Institute for Meteorology, Leipzig, Germany
[3]Fraunhofer Institute for Energy Economics and Energy System Technology, Kassel, Germany
[4]Geophysical Institute, University of Bergen, Bergen, Norway
[5]Bjerknes Center for Climate Research, Bergen, Norway

Correspondence: Fiona Paulus (fpaulus@uni-koeln.de)

Abstract.

The impact of mesoscale vertical motion on the thermodynamic, microphysical, and convective transformations of marine cold air outbreaks (MCAOs) is still largely unknown, partly due to scarce high-resolution observations in upstream Arctic regions. Therefore, this study investigates the effects of mesoscale subsidence on the evolution of the atmospheric boundary-layer (ABL), cloud phase, and precipitation for a case study of a shallow MCAO observed in the Fram Strait in March 2022 during the HALO–(AC)3 campaign. Quasi-Lagrangian large-eddy simulations (LES) are conducted with observational initialisation and larger-scale forcing, based on airborne in-situ and remote-sensing measurements. The LES control simulation accurately reproduces the measured thermodynamic ABL structure and the temporal evolution of the observed air mass moving over the Arctic sea ice onto the open ocean. Specifically, the measured ABL height, integrated water vapour, and cloud water paths are well represented by the LES. Sensitivity experiments using the LES with prescribed subsidence reveal that weaker subsidence substantially alters the evolution of cloud phase during the MCAO, featuring a deeper ABL and an earlier onset of cloud glaciation. This study shows that ABL internal decoupling plays a key role in this process. Decoupling occurs sooner under weaker mesoscale subsidence, triggering convective graupel formation that subsequently intensively converts liquid water droplets. This strong link between glaciation and decoupling arguably explains the typical evolution of the cloud liquid water path observed in many MCAOs. These results provide a process-based framework for interpreting the role of large-scale vertical motion in Arctic air mass transformations.

1 Introduction

During marine cold air outbreaks (MCAOs), cold and dry Arctic air masses move southward over the cold sea ice surface towards the warmer open ocean, where they heat up and pick up humidity from below. These MCAOs are an essential phenomenon in the Arctic climate system that frequently occurs over extended marine regions at northern high latitudes (Fletcher et al., 2016). Additionally, as these air masses cross the sea ice edge and move over open ocean, the strong near-surface

https://doi.org/10.5194/egusphere-2026-554
Preprint. Discussion started: 11 February 2026

temperature contrast between the warmer open ocean surface and the overlaying colder air generates intense turbulent and convective mixing, producing large sensible heat fluxes (Shapiro et al., 1987; Renfrew and Moore, 1999; Papritz et al., 2015; Kirbus et al., 2023). This vertical turbulent exchange rapidly transforms the air mass from below, deepening the Atmospheric Boundary Layer (ABL) through convection. As a result, spatially organised cloud structures evolve in the ABL that initially appear as cloud streets (Atkinson and Wu Zhang, 1996; Lenschow and Agee, 1976; Etling and Brown, 1993; Kirbus et al., 2024; Klingebiel et al., 2025). As the air mass continues to respond to the warm open ocean surface, lower-level warming and moistening, together with persistent vertical surface energy flows, precipitation, and cloud microphysical processes such as riming and secondary ice production, may cause a transition from cloud streets to deeper, broken cloud fields (Tornow et al., 2021; Murray-Watson et al., 2023; Schirmacher et al., 2024). These evolving cloud and ABL characteristics modulate cloud-radiative interactions, determine precipitation formation, increase surface winds, and can generate polar lows (Kolstad, 2017; Terpstra et al., 2021; Mateling et al., 2023). Through this ocean–atmosphere coupling, MCAOs can also influence atmospheric and oceanic circulations (Rasmussen et al., 1992; Isachsen et al., 2013; Papritz and Spengler, 2017; Marcheggiani and Spengler, 2025), which are linked to feedback mechanisms of Arctic amplification. The air mass transports during MCAOs and the corresponding transformation processes may also contribute to heat and moisture exchange between the Arctic and mid-latitudes (Pithan et al., 2018).

Despite extensive prior studies, key aspects of MCAO evolution remain poorly understood, particularly the onset of ABL decoupling in the subcloud layer, which accelerates stratocumulus breakup and promotes transitions between cloud regimes (Bretherton and Wyant, 1997; McCoy et al., 2017; Lloyd et al., 2018; Zhou et al., 2015). Furthermore, precipitation and cloud microphysical developments that are influenced by riming and secondary ice production, reducing vertical mixing and altering ABL energy budgets, are not well represented in models (Abel et al., 2017; Karalis et al., 2022; Wu et al., 2025). Persistent observational gaps, particularly in remote upstream regions of MCAO pathways, continue to limit our understanding of these processes and their role in organising MCAO transitions. Consequently, major questions remain regarding how dynamical and microphysical processes support the transition to open-cell convection and how these should be represented in numerical models (Tomassini et al., 2017; de Roode et al., 2019).

The role of mesoscale vertical motion in MCAO evolution, and mixed-phase clouds in particular, is complex and not yet fully understood. Previous studies have shown that subsidence in surface-coupled convective layers strengthens the capping temperature inversion by counteracting top entrainment, thus increasing ice and liquid water path below. In return, enhanced cloud-top radiative cooling and convective overturning under stronger subsidence can increase precipitation production in both rain and snow, stabilising stratiform cloud layers by suppressing cloud-top ascent and prolonging cloud persistence (Young et al., 2018). In contrast, Neggers et al. (2019) found that strong subsidence can cause mixed-phase cloud layers over the central Arctic sea ice to collapse, shifting thermal-infrared radiative cooling to the surface and hindering cloud reformation. These findings highlight that mesoscale subsidence can strongly modulate mixed-phase cloud layers, but it remains unknown how this modulation depends on the ABL structure. The involved interactions span a wide range of spatial scales, from mesoscale to synoptic subsidence. It covers processes such as turbulent entrainment, microphysical processes, and aerosol particle evolution (Tornow et al., 2021, 2023). A prime cause for our lack of insight into the impact of mesoscale subsidence on mixed-phase

https://doi.org/10.5194/egusphere-2026-554
Preprint. Discussion started: 11 February 2026

clouds is the distinct observational data gap on this variable at high latitudes. Measuring large-scale vertical motion or horizontal divergence remains difficult, as small errors in horizontal wind gradients lead to large uncertainties when using mass conservation. A more robust method applies regression to dropsonde data released in mesoscale patterns by fast aircraft, pioneered during two aircraft campaigns in the subtropical trades (Bony and Stevens, 2019; Stevens et al., 2021; George et al., 2021). The application of this method to the coherent flow of an Arctic MCAO, can help to narrow this data gap and enhance our understanding of the impacts of subsidence on the development of mixed-phase clouds in growing boundary layers.

The Fram Strait is a hotspot for MCAOs. It is relatively easy to access, making it a frequent target area for atmospheric observational and modelling studies. Although many recent Fram Strait studies are model-based, several field campaigns have filled key data gaps of MCAO processes. For example, the Cold air Outbreaks in the Marine Boundary Layer Experiment (COMBLE) campaign in 2019 and 2020 observed several MCAOs with two permanent observational sites that provided continuous measurements in the Fram Strait region (Geerts et al., 2022), and the Springtime Atmospheric Boundary Layer Experiment (STABLE) campaign in March 2013 provided airborne observations with a research aircraft in the Fram Strait (Michaelis et al., 2022). The HALO–$(\mathcal{AC})^3$campaign in 2022 sampled numerous MCAOs with multiple co-located aircraft, probing upstream and downstream regions (Walbröl et al., 2024; Wendisch et al., 2024; Ehrlich et al., 2025; Wendisch et al., 2025). During HALO–$(\mathcal{AC})^3$, the mesoscale dropsonde pattern technique was applied to sample subsidence at multiple points along a MCAO trajectory for two consecutive days, producing the first robust high-latitude subsidence dataset of its kind (Paulus et al., 2024). This unique dataset creates new opportunities for investigating the role of subsidence in MCAO evolution.

The main objective of this study is to use quasi-Lagrangian Large-Eddy Simulations (LES), driven by HALO–$(\mathcal{AC})^3$ observational data, to gain insight into the impacts of mesoscale subsidence on MCAOs. For a particular case study, the LES follows an observed MCAO along its two-day southbound trajectory, initialised with in-situ dropsonde profiles from the High Altitude and Long Range Aircraft (HALO) in the far north. The simulated air mass evolves freely, with large-scale forcings, including vertical motion, geostrophic wind, and advection tendencies, derived from circular dropsonde pattern observations and prescribed along the trajectory (Paulus et al., 2024). The simulated ABL and cloud properties are compared against independent downstream aircraft observations.

Given this observationally constrained setup, we ask how well the Lagrangian LES reproduces the independently observed cloud development. After evaluating the model performance, we conduct perturbation experiments on the mesoscale subsidence to assess the sensitivity of the MCAO, focusing on the evolution of the ABL structure, cloud mass, thermodynamic phase, and surface precipitation. This study aims to discuss how microphysical and dynamical properties and processes interact in their response to perturbed larger-scale subsidence forcing within the simulated MCAO system.

2 Observations

2.1 The HALO–$(\mathcal{AC})^3$ campaign

The HALO–$(\mathcal{AC})^3$ field campaign took place from March to April 2022 in the Arctic west of Norway and the Fram Strait. The main objective of this campaign was to understand the transformation of air masses between the Arctic and the mid-latitudes

https://doi.org/10.5194/egusphere-2026-554
Preprint. Discussion started: 11 February 2026

and to investigate the influence of these interactions on ABL processes and cloud formation. To this end, a quasi-Lagrangian sampling strategy was applied during the campaign, in which the transformation of individual air parcels of an air mass was tracked along their trajectories using three research aircraft flying at different altitudes (HALO, Polar 5 (P5) and Polar 6) (Wendisch et al., 2024). An overview of the synoptic situation during the HALO–$(\mathcal{AC})^3$ campaign is provided by Walbröl et al. (2024).

This study focuses on a case study analysing two HALO Research Flights (RF10 and RF11) conducted on the two days of March 29, 2022 and March 30, 2022 respectively (Figure 1). On these two days, a weak MCAO with an MCAO index of four was investigated (Papritz and Spengler, 2017; Walbröl et al., 2024) (Appendix A). Both days were characterised by a persistent, steady, and relatively slow northerly wind of about 3 to $10\,\mathrm{m\,s^{-1}}$ measured at $10\,\mathrm{m}$ altitude by dropsonde observations. These MCAO characteristics define a weak MCAO compared to climatological MCAO values from the Fram Strait (Slättberg et al., 2025)). The slowly moving air mass was in the range of HALO during the investigated period of two days. The observed MCAO case occurred during a cold period between two intervals of strong MCAOs from March 21–26, 2022 and April 1–2, 2022 (Walbröl et al., 2024).

The synoptic situation in the Fram Strait was characterised by a high-pressure system with its centre located at the east coast of Greenland and a low-pressure area in the Barents Sea. The cloud field was dominated by shallow convective mixed-phase clouds, with clearly defined street features near the sea ice edge. These streets broke up further downstream of the flow in the area of C03 (Figure 1), where the cloud cover increased significantly. A notable cloud-free area was located on the west coast of Svalbard (Figure 2), which can be attributed to the foehn effect during easterly flow over Svalbard, similarly observed during other field campaigns (e.g. Shestakova et al., 2022).

The HALO flight plans on these two days were created by tracking the location of an air mass sampled on the first day at a location in the high north using trajectory estimates based on forecast data. At four locations along the trajectory, the air mass was sampled using a circular mesoscale dropsonde pattern, each time with a diameter of $150\,\mathrm{km}$. This technique is inspired by Lenschow et al. (2007) and has previously been applied in the North Atlantic and subtropical region by Stevens et al. (2019, 2021) to measure mesoscale divergence and subsidence profiles. The centre of the initial circle (IC) (Figure 1) on the first day at 14:00 UTC was located at ($84.4\,^\circ$N, $13.6\,^\circ$E) and featured only five dropsondes, a number limited by airspace restrictions. On the second day, three further circles were flown along the predicted southern trajectory of the air mass. The circles sampled during the two subsequent days each featured eight evenly distributed dropsondes, with two additional dropsondes launched in their inner areas. Only one of the day-two circles, (C02) at ($78.6\,^\circ$N, $4.0\,^\circ$E, at 11:30 UTC), was located at the exact predicted location of the air mass as sampled on the previous day at the IC location. As shown in Figure 1, this circle was situated over open ocean. Two further circles were flown on day two, one (C01) further upstream over sea ice ($80.8\,^\circ$N, $10.7\,^\circ$E, at 10:30 UTC), and another (C03) was flown at a downstream location at a similar distance ($76.3\,^\circ$N, $3.3\,^\circ$E, at 12:30 UTC). The P5 aircraft took additional measurements in the C02 area, shortly after the departure of the HALO aircraft from this area (at 12:00 UTC), using a rectangular flight pattern with three cross-flow legs. Additional measurements were conducted by a controlled meteorological balloon (CMET) launched from Ny-Ålesund, as part of the ISLAS2022 field experiment, which took place at the same time as the HALO–$(\mathcal{AC})^3$campaign.

https://doi.org/10.5194/egusphere-2026-554
Preprint. Discussion started: 11 February 2026

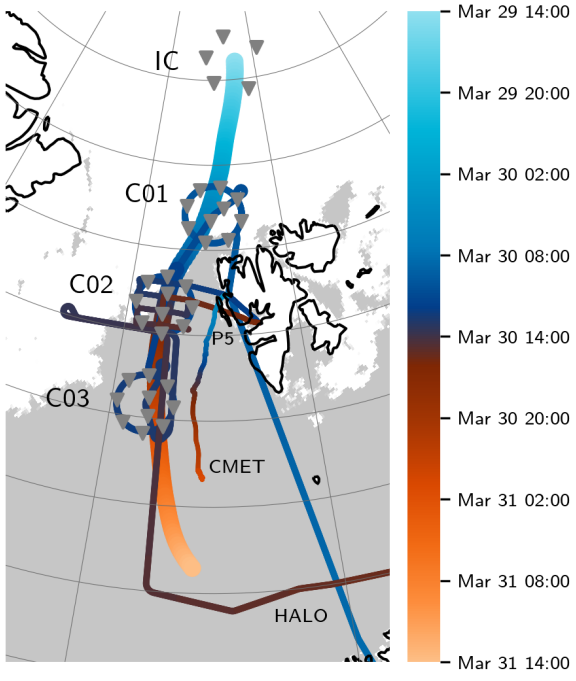

Figure 1. Map of the simulation trajectory for the Lagrangian LES (bold line) initiated in the centre of the circular flight leg on March 29, 2022 of the HALO–$(\mathcal{AC})^3$ campaign, together with the flight paths of the HALO and P5 aircraft on March 30, 2022 and the trajectory of the CMET. Locations where dropsondes were released in IC on March 29, 2022 and in C01, C02 and C03 of March 30, 2022 from HALO are indicated by ▼. The sea ice concentration retrieved from satellite observations (Spreen et al., 2008) is indicated in grey and white, and the colour bar denotes the time (UTC) along the trajectory and flight paths.

2.2 Observational datasets

This study uses a combination of in-situ and remote sensing observations from the HALO–$(\mathcal{AC})^3$ campaign to constrain the LES experiments and evaluate the model performance. A comprehensive overview of the measurements collected during HALO–$(\mathcal{AC})^3$ is described by Ehrlich et al. (2025), and a summary of the datasets used is presented in Table 1, including the variable names, associated instruments, and references to more detailed technical and scientific descriptions.

The deployed Vaisala RD-41 dropsondes provide vertical profile measurements of the thermodynamic state, including air temperature at a resolution of $0.01\,\mathrm{K}$, air humidity at a resolution of $0.1\,\%$ and air pressure at a resolution of $0.01\,\mathrm{hPa}$ at frequencies between 2 and $4\,\mathrm{Hz}$ and descend at speeds between 10 and $20\,\mathrm{m\,s^{-1}}$ (Vaisala, 2023). The measured profiles are interpolated to a uniform vertical grid of $5\,\mathrm{m}$ spacing. The horizontal wind speed profiles were determined from GPS data with an estimated accuracy of $0.1\,\mathrm{m\,s^{-1}}$ (Hock and Franklin, 1999; Wang et al., 2015). These observations were used to derive vertical profiles of subsidence (Figure 3), geostrophic wind, and advective tendencies of temperature, humidity, and

https://doi.org/10.5194/egusphere-2026-554
Preprint. Discussion started: 11 February 2026

wind through a regression algorithm applied to the dropsondes deployed in each circle. A comprehensive description of the calculation technique is provided by Paulus et al. (2024).

To constrain the surface skin temperature T_{skin}, airborne measurements of the thermal infrared imager on board HALO VELOX (Video airbornE Longwave Observations within siX channels; Schäfer et al., 2022) were used, which records two-dimensional fields ($640 \times 512\,\text{pixel}$) of the thermal infrared brightness temperature. At typical HALO flight altitudes, this corresponds to a horizontal resolution of $10\,\text{m}$ with a temporal resolution of $1\,\text{Hz}$ for a field-of-view of $6.4 \times 5.1\,\text{km}$. From these brightness temperature images, we retrieve T_{skin} and sea-ice concentration along the circular flight legs of HALO with accuracies of $1.2\,\text{K}$ and $5\,\%$, respectively (Müller et al., 2025). For partly cloudy open-ocean segments in C02 and C03, we apply a cloud mask and classify pixels whose retrieved T_{skin} exceeds $-1.8\,^{\circ}\text{C}$ above the surrounding (cloudy) background as open ocean. The final surface skin temperature is the horizontal mean of each masked 2D-field at a $1\,\text{Hz}$ time resolution.

The observational datasets collected during the HALO–$(\mathcal{AC})^3$ campaign provide all atmospheric state variables required to run Lagrangian LES experiments following the air mass as it moves south. A small number of surface parameters, specifically surface albedo, the aerodynamic roughness length for momentum, and the thermal roughness length for heat, could not be observed, but are needed to prescribe the (latitude-dependent) surface boundary condition in the LES experiments. Therefore, these data were retrieved from the European Centre for Medium-Range Weather Forecasts (ECMWF) reanalysis product version 5 (ERA5; Hersbach et al. (2020)). By combining the dropsonde and VELOX observations with the surface values from ERA5, a complete set of forcing fields for the Lagrangian LES has been compiled.

For model validation, independent datasets also obtained from the HALO–$(\mathcal{AC})^3$ campaign are used. The Airborne Mobile Aerosol Lidar (AMALi) on the P5 aircraft provides measurements of cloud top height, which are compared to the simulated cloud top heights (Stachlewska et al., 2009). The liquid water and ice water paths are derived from the Microwave Radar/Radiometer for Arctic Clouds (MiRAC) on board P5 (Mech et al., 2019). The ice water path is derived from the $94\,\text{GHz}$-radar reflectivity using the Ze–IWC relationship of Hogan et al. (2006). We additionally include integrated water vapour IWV and liquid water path LWP data retrieved from the HALO Microwave Package (HAMP) over open ocean (not available over sea ice) (Mech et al., 2014). The additional data allows a direct comparison with the quantities computed by the LES.

Further thermodynamic observations were performed using Lagrangian CMET soundings (Voss et al. (2010); Løklingholm et al. (2026), manuscript to be submitted). The balloon was equipped with an air temperature sensor that operates over a range of -40 to $105\,^{\circ}\text{C}$ with an interchangeability of $\pm 0.5\,^{\circ}\text{C}$ and measured relative humidity with respect to water with an accuracy of $1.5\,\%$. Due to the cold, dry conditions, and the absence of active ventilation of the sensor package on the CMET, actual measurement errors would be substantially larger than the sensor interchangability, in particular during daytime when the balloon was drifting horizontally, creating an overall warm and dry bias (Løklingholm et al., 2026). This particular CMET-04 was launched in Ny-Ålesund on March 30, 2022 at 14:00 UTC following a trajectory parallel to the simulated trajectory (Figure 1), complementing the dropsonde observations and providing additional in-situ validation data within the lower ABL.

https://doi.org/10.5194/egusphere-2026-554
Preprint. Discussion started: 11 February 2026

Table 1. Variables used in the LES for initialisation (I), evaluation (E), boundary condition (BC) and larger scale forcing (F).

Variable	Unit	Description	Instrument	Platform	Reference	Usage
T	K	Air temperature	Dropsonde, CMET	HALO, CMET	Vaisala (2023); Voss et al. (2010)	I,E
q	$\mathrm{kg\,kg^{-1}}$	Dpecific humidity				I,E
p	hPa	Pressure	Dropsonde	HALO	Vaisala (2023)	I,E
u, v	$\mathrm{m\,s^{-1}}$	Horizontal wind components				I
$-\boldsymbol{v}_h \cdot \nabla T$	$\mathrm{K\,s^{-1}}$	Advection of air temperature	Regression from Dropsondes	HALO	Paulus et al. (2024)	F
$-\boldsymbol{v}_h \cdot \nabla q$	$\mathrm{kg\,kg^{-1}\,s^{-1}}$	Advection of specific humidity				F
$-\boldsymbol{v}_h \cdot \nabla u, -\boldsymbol{v}_h \cdot \nabla v$	$\mathrm{m\,s^{-2}}$	Advection of meridional/zonal wind				F
u_g, v_g	$\mathrm{m\,s^{-1}}$	Geostrophic wind				F
w	$\mathrm{m\,s^{-1}}$	Subsidence				F
T_{skin}	K	Surface skin temperature	VELOX	HALO	Müller et al. (2025)	BC
sic	%	Sea ice fraction				BC
α		Surface albedo	ERA5	ERA5	Hersbach et al. (2020)	BC
z_0	m	Roughness length for momentum				BC
$z_{0,h}$	m	Roughness length for heat				BC
z_c^t	m	Cloud top height	AMALi	HALO	Stachlewska et al. (2009)	E
IWV	$\mathrm{kg\,m^{-2}}$	Integrated water vapour	HAMP	HALO	Mech et al. (2014)	E
LWP	$\mathrm{g\,m^{-2}}$	Liquid water path	HAMP, MiRAC	HALO, P5	Mech et al. (2014, 2019)	E
IWP	$\mathrm{g\,m^{-2}}$	Ice water path	MiRAC	P5	Mech et al. (2019)	E

https://doi.org/10.5194/egusphere-2026-554
Preprint. Discussion started: 11 February 2026

3 Model configuration

3.1 The Dutch Atmospheric Large-Eddy Simulation Model (DALES)

The simulations were performed using the Dutch Atmospheric Large-Eddy Simulation (DALES) (Heus et al., 2010), which is an open-source model available at https://github.com/dalesteam/dales. DALES has been used extensively in previous scientific studies of ABL turbulence and clouds in various regions of the Earth (van der Dussen et al., 2013; Corbetta et al., 2015; Roode et al., 2016; Laar et al., 2019; Reilly et al., 2020), including the Arctic (Neggers et al., 2019; de Roode et al., 2019; Egerer et al., 2021; Chylik et al., 2023; Schnierstein et al., 2024).

To represent Arctic mixed-phase clouds, the DALES code was equipped with the double-moment microphysics scheme of Seifert and Beheng (2006), which is predictive of both the mass and number concentrations of five hydrometeor types (cloud water, cloud ice, rain, snow, and graupel) (Neggers et al., 2019; Chylik et al., 2023). The number concentration of cloud condensation nuclei (CCN) is prognostic, initialised with a constant vertical profile of $100\,\mathrm{cm}^{-3}$ within the range observed during the HALO–$(\mathcal{AC})^3$ campaign in the Fram Strait (Wendisch et al., 2024) and in the high Arctic during MOSAiC (Ansmann et al., 2023). The number concentration of ice nucleating particles (INPs) is prescribed at a value of $1 \times 10^{-3}\,\mathrm{cm}^{-3}$, following Hartmann et al. (2019). Heterogeneous freezing processes are limited to temperatures below $-15\,^{\circ}\mathrm{C}$, and the maximum number of ice particles resulting from deposition nucleation is restricted to $200\,\mathrm{L}$, while homogeneous freezing and secondary ice formation via the Hallett-Mossop process remain unchanged as represented in the Seifert and Beheng (2006) model. This microphysical model setup was thoroughly tested by Schnierstein et al. (2024) against a year of in-situ measurements of Arctic clouds in the central Arctic during the MOSAiC expedition.

Further model settings follow the setup described by Schnierstein et al. (2024). They include a radiative transfer scheme interactive with liquid and ice hydrometeors applying a four-stream radiative transfer solver in combination with Monte Carlo spectral integration (Pincus and Stevens, 2009). The optical properties of ice particles are based on the physical properties of the ice crystals derived from the microphysics scheme (McFarquhar and Heymsfield, 1998; Fu and Liou, 1993; Baran, 2005; Schnierstein et al., 2024). Resolved advection is calculated using a fifth-order central difference numerical scheme for momentum and a κ-limiter scheme for the other prognostic scalar variables. Subgrid-scale transport uses a prognostic turbulent kinetic energy (SFS-TKE) scheme (Deardorff, 1980; Hundsdorfer et al., 1995). A sponge layer is applied in the upper $25\,\%$ of the range to dampen disruptive gravity waves. The surface fluxes of heat, moisture, and momentum are calculated based on Monin-Obukhov theory using Arctic stability functions derived by Grachev et al. (2007). Horizontally periodic boundary conditions are applied, while large-scale forcings are prescribed as time-dependent tendency profiles to account for advection, subsidence, and horizontal pressure gradients (geostrophic wind vector $\boldsymbol{v}_g$).

3.2 Trajectory calculation

To set up a Lagrangian LES experiment, the trajectories (pathways) of the air parcels forming the air mass need to be estimated. As described in Section 2.1, trajectories for the low-level air parcels were calculated during flight planning using the Lagrangian Analysis Tool (LAGRANTO) (Sprenger and Wernli, 2015) and based on IFS forecast winds. For this study, this was repeated

https://doi.org/10.5194/egusphere-2026-554
Preprint. Discussion started: 11 February 2026

using three-dimensional wind fields of the ERA5 reanalysis. Air parcels were identified, and their trajectories were calculated starting every 3 km lat/lon within the IC on March 29, 2022 and matching the circle locations on March 30, 2022 (Kirbus et al., 2024). The best match of the trajectories was found at 870 hPa in the initiation region. For the simulations, a mean trajectory was calculated by averaging all trajectories initiated within the first circle at 870 hPa. Each trajectory is included for every circle region it intersects, but is excluded from further analysis once it exits a circle region without entering the subsequent one. This procedure is illustrated in Figure A2.

3.3 Observational forcing and boundary conditions

The lower boundary condition consists of a prescribed surface skin temperature T_{skin} based on VELOX measurements (Section 2.2). These observations are averaged longitudinally and interpolated along the simulation trajectory and constrain the surface boundary of the LES (Figure 2). The lower boundary condition for atmospheric specific humidity was computed as the saturation humidity based on the surface skin temperature and the corresponding sea ice fraction within the LES model.

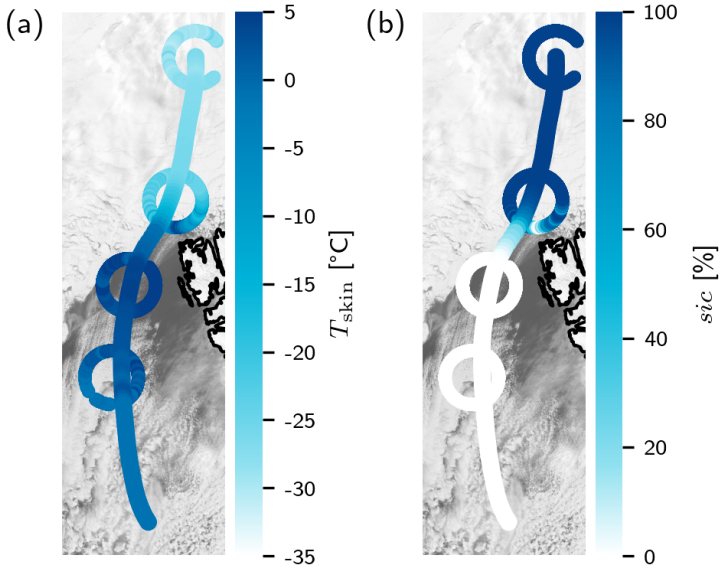

Figure 2. VELOX observations of surface skin temperature (T_{skin}) and sea ice concentration sic on the circular flight legs of the HALO flights on March 29, 2022 and March 30, 2022 during HALO–$(\mathcal{AC})^3$ (circles), together with interpolated T_{skin} and sic along the LES trajectory used as surface boundary conditions (bold line).

The prescribed large-scale forcing profiles are time-dependent and they are obtained by interpolation along the trajectory between the sonde data at the four circle locations. A regression algorithm is used to estimate horizontal gradients within each circle area, following the method of Bony and Stevens (2019). The horizontal wind divergence and the associated subsidence ω are calculated as described by Paulus et al. (2024). At high latitudes, Cartesian latitude–longitude coordinates distort hori-

https://doi.org/10.5194/egusphere-2026-554
Preprint. Discussion started: 11 February 2026

zontal distances. To address this issue, Paulus et al. (2024) introduced a regression method in spherical coordinates $[r, \varphi, \vartheta]$. Assuming linear fluctuations of any variable $\xi \in [u, v, q, T, p]$ within the dropsonde area, ξ at the centre of the pattern can then be approximated at every vertical level by a first-order Taylor expansion:

$$\xi = \xi_0 + \frac{\partial \xi}{\partial \vartheta} \Delta\vartheta + \frac{\partial \xi}{\partial \varphi} \Delta\varphi \,. \tag{1}$$

Here, ξ_0 denotes the mean of all dropsonde measurements, and ϑ and φ are the polar and azimuth angles, respectively. This approach is applied in this study to estimate divergence:

$$D = \boldsymbol{\nabla} \cdot \boldsymbol{v}_h = \frac{1}{r \cdot \sin\vartheta} \left[\frac{\partial u}{\partial \varphi} + \frac{\partial \sin\vartheta \, v}{\partial \vartheta} \right] . \tag{2}$$

This allows for the estimation of the associated subsidence at height z by vertical integration from the surface:

$$\omega = -g \cdot \varrho \int_0^z D \, \mathrm{d}z \,. \tag{3}$$

Figure 3 shows the resulting subsidence profiles in the four circles, provided in pressure and height units for reference, with key characteristics summarised in Table B1. In IC and C02, subsidence dominates the lowest $3\,\mathrm{km}$, with mean downward motions of -0.74 and $-0.60\,\mathrm{cm\,s^{-1}}$, respectively, while C03 exhibits weaker subsidence throughout the profile. In contrast, C01 shows a mean upward motion over the $8\,\mathrm{km}$ profile. Uncertainties were estimated following Paulus et al. (2024) and reach up to $0.025\,\mathrm{cm\,s^{-1}}$ ($0.002\,\mathrm{Pa\,s^{-1}}$) below $3\,\mathrm{km}$ across all circles, which cannot be resolved in the figure and are therefore not shown. The subsidence magnitudes are consistent with reanalysis-based estimates of Arctic MCAOs (Paulus et al., 2024; Tornow et al., 2023), but are approximately an order of magnitude lower than those reported for the tropical Atlantic, possibly due to the specific weather conditions of the sampled case (Bony and Stevens, 2019; George et al., 2021).

The same regression approach using spherical coordinates can be applied to calculate the horizontal advective tendencies in the circular areas,

$$-\boldsymbol{v}_h \cdot \boldsymbol{\nabla}\xi = -\left[u \frac{1}{r} \frac{\partial \xi}{\partial \vartheta} + \frac{1}{r \cdot \sin\vartheta} \frac{\partial \xi}{\partial \varphi} \right] , \tag{4}$$

and similarly, the horizontal pressure gradient force, here expressed as the geostrophic wind vector $\boldsymbol{v}_g$,

$$\boldsymbol{v}_g = \frac{1}{\varrho \cdot f} \cdot \begin{pmatrix} \frac{\partial p}{\partial \varphi} \\ \frac{1}{\cos\varphi} \frac{\partial p}{\partial \vartheta} \end{pmatrix} . \tag{5}$$

These profiles, which extend up to HALO's flight altitude at about $8\,\mathrm{km}$, are linearly interpolated between the four circles and kept constant south of the last circle along the simulation trajectory (Figure 4). What stands out in the interpolated mesoscale vertical pressure velocity field $\omega(t, z)$ is the distinct maximum at C02 below $4\,\mathrm{km}$, which indicates a relatively strong signal in the prescribed subsidence that will play a crucial role in this study. Concerning the advective tendencies, the temperature advection $-\boldsymbol{v}_h \cdot \boldsymbol{\nabla} T$ is dominated by cooling at low altitudes, below $1\,\mathrm{km}$. The specific humidity exhibits low-level drying before the sea ice edge, transitioning to moistening south of C02. The horizontal wind components show low signals, except

https://doi.org/10.5194/egusphere-2026-554
Preprint. Discussion started: 11 February 2026

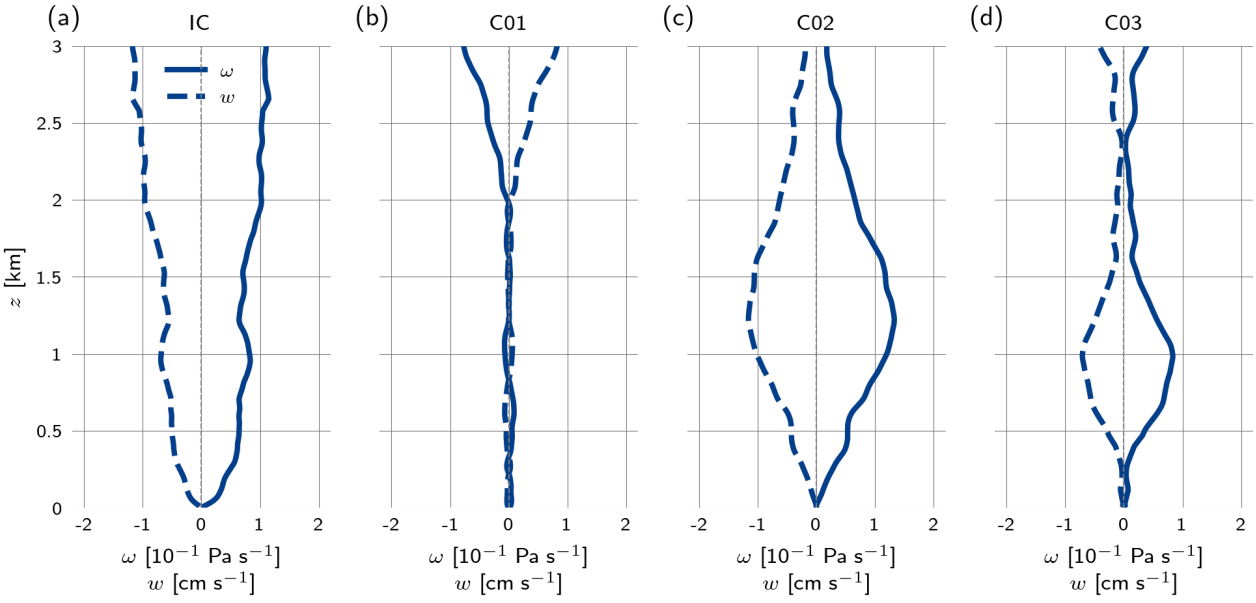

Figure 3. Subsidence profiles obtained through regression from a dropsonde pattern in pressure (ω, solid line) and height (w, dashed line) coordinate for all dropsonde patterns on March 29, 2022 and March 30, 2022 of the HALO–$(\mathcal{AC})^3$ campaign. Associated uncertainty estimates cannot be resolved in the figure and are discussed in the main text.

for a slight positive tendency of the meridional wind in the deepening ABL south of C01. These likely reflect Ekman-layer effects of Reynolds stresses, inducing a deviation of the wind from the geostrophic wind direction. The geostrophic wind ($|\boldsymbol{v}_g|$) expresses an eastward zonal pressure gradient force throughout the lower levels, consistent with the general synoptic situation during the two days. It should be noted that at a trajectory height of $870\,\mathrm{hPa}$ corresponding to heights between $1.34\,\mathrm{km}$ and $1.38\,\mathrm{km}$, advective tendencies are, by definition, zero, as the air mass speed is subtracted from the wind in the Lagrangian forcing method.

Above $8\,\mathrm{km}$ altitude, which is well above the simulated ABL height (max $2\,\mathrm{km}$), the sonde data are extended by ERA5 fields. The main objective of this procedure is to allow radiative flux density (irradiance) calculations above the model domain in which turbulence is resolved, which has a ceiling far below HALO's flight altitude (described in Section 3.4). As a result, it is concluded that the use of ERA5 fields above this height has no discernible impact on the model results.

3.4 Experimental setup

Apart from the control setup, four additional LES experiments are conducted using DALES to investigate the sensitivity of ABL evolution to the mesoscale subsidence forcing. The experimental setup includes (i) the control simulation (Ctrl) that employs the observed subsidence (Section 3.3), (ii) a simulation without subsidence (NoSub) to isolate the effects of entrainment on ABL development, and (iii) further experiments in which observed subsidence was scaled by $10\,\%$ (Sub10), $50\,\%$ (Sub50)

https://doi.org/10.5194/egusphere-2026-554
Preprint. Discussion started: 11 February 2026

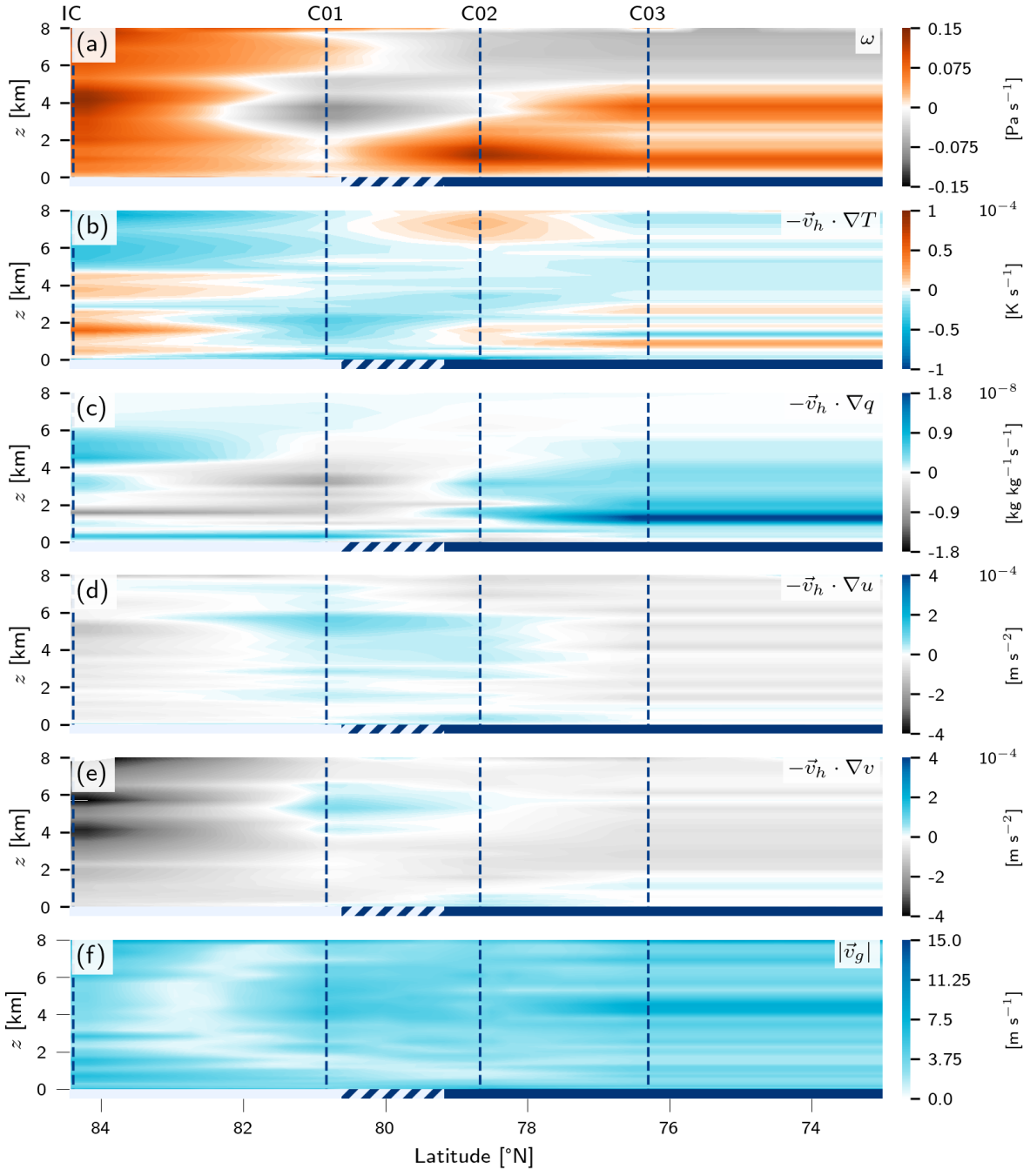

Figure 4. Simulation forcing of subsidence ω (Ctrl) (a), horizontal temperature advection $-\boldsymbol{v}_h \cdot \nabla T$ (b), horizontal humidity advection $-\boldsymbol{v}_h \cdot \nabla q$ (c), horizontal advection of the zonal and meridional wind components $-\boldsymbol{v}_h \cdot \nabla u$ (d), $-\boldsymbol{v}_h \cdot \nabla v$ (e), and the geostrophic wind magnitude $|\boldsymbol{v}_g|$ (f). All fields are interpolated between dropsonde observation locations IC, C01, C02 and C03 (dashed blue lines). The surface cover is indicated at the bottom of each subfigure as sea ice ($sic > 0.9$, light blue), marginal sea-ice zone ($0 < sic \leq 0.9$, hatched), and open ocean ($sic = 0$, dark blue).

https://doi.org/10.5194/egusphere-2026-554
Preprint. Discussion started: 11 February 2026

and 200 % (Sub200). These scaling factors correspond to a range of subsidence rates covering weaker values ($-0.12\,\mathrm{cm\,s^{-1}}$) comparable to those used in LES studies of mixed-phase Arctic clouds (Solomon et al., 2018; Young et al., 2018), up to stronger rates of approximately $-2.3\,\mathrm{cm\,s^{-1}}$, and consistent with observations during the EUREC^{4}A campaign in the tropics (Poujol and Bony, 2024). In all sensitivity experiments, the temporal and vertical structure of the observed subsidence was retained, while only its magnitude was modified.

The model domain spans $12.8\,\mathrm{km} \times 12.8\,\mathrm{km}$ with $50\,\mathrm{m}$ horizontal resolution and 191 vertical levels, starting at $10\,\mathrm{m}$ with $20\,\mathrm{m}$ spacing up to $2.1\,\mathrm{km}$ and increasing resolution aloft to a ceiling height of $6.8\,\mathrm{km}$ with maximum grid spacing of $177\,\mathrm{m}$. Periodic horizontal boundaries are applied, and large-scale forcings are horizontally homogeneous but variable in time and height along the trajectory. The prescribed subsidence acts on the evolving model profile. Continuous Newtonian nudging towards the observed profiles of $\{T, q, u, v\}$ is applied above the ABL, determined by the strongest inversion in liquid water potential temperature, with a buffer layer of $100\,\mathrm{m}$ where the nudging time scale increases linearly up to $3\,\mathrm{h}$. Nudging increases in the upper quarter of the domain to suppress gravity waves, while below the ABL, the flow evolved freely. Each experiment is $45\,\mathrm{h}$ long, reaching the marginal sea ice zone approximately $15\,\mathrm{h}$ after initialisation.

4 Results I: Evaluation of the control simulation

In this section, we evaluate the performance of the control (Ctrl) LES in reproducing key characteristics of the MCAO observed on March 29, 2022 and March 30, 2022 during the HALO–$(\mathcal{AC})^3$campaign. We analyse the evolution of cloud liquid and ice water contents and paths, the vertical structure and evolution of the ABL height, air temperature and humidity profiles along the simulation trajectory, and the associated turbulent heat energy fluxes. As outlined in Section 2, observations from dropsondes, lidars, and radiometers are used to assess the model's ability to capture the spatial and temporal variability of the atmosphere, and the representation of turbulent and thermodynamic processes.

4.1 Atmospheric boundary layer and cloud evolution

First, we examine the evolution of the ABL and clouds, focusing on the temporal development of cloud liquid and ice water contents as well as the deepening of the ABL along the simulation trajectory of the MCAO, expressed as a function of latitude in Figure 5. The initial atmospheric column at circle IC includes a shallow ABL of $65\,\mathrm{m}$, which remains low over the sea ice in the simulation. The ABL begins to deepen once it reaches the marginal sea ice zone (MIZ) where warmer surface conditions trigger enhanced vertical latent and sensible heat fluxes. Convective updrafts form a thin mixed-phase cloud between C01 and C02, with ice reaching to the surface and a shallow liquid layer existing near the cloud top during the initial phase of the growing ABL. As the air mass moves over the open ocean, the ABL continues to deepen, reaching values of liquid water content q_l up to $0.35\,\mathrm{g\,kg^{-1}}$. At the end of the $45\,\mathrm{h}$ simulation, the ABL has grown to approximately $1.5\,\mathrm{km}$.

To evaluate the Ctrl simulation with respect to the ABL structure, several independent measurements of ABL height are compared with the simulation output. The ABL height was determined from dropsonde profiles using the Bulk Richardson number Ri_b, which quantifies the balance between buoyancy and shear (Stull, 1988). A critical threshold $Ri_b^{\mathrm{crit}} = 0.25$ was

https://doi.org/10.5194/egusphere-2026-554
Preprint. Discussion started: 11 February 2026

used to define the height of the ABL z_i, consistent with the diagnostics of the IFS CY43R1 model and the ERA5 reanalysis (ECMWF, 2016; Seidel et al., 2012). Lidar measurements from the P5 aircraft (AMALi) provide cloud top height (z_c^t), which is comparable to the ABL height in MCAO cases due to the strong coupling of ABL growth to cloud development. Finally, the simulation diagnoses the height of the ABL from the minimum flux of total liquid water potential temperature (Stevens et al., 2001), $\overline{w'\vartheta_l'}$, within the lowest $3\,\mathrm{km}$ of the domain. AMALi measured a mean cloud top height of $0.63 \pm 0.11\,\mathrm{km}$ at location C02, yielding an RMSE of $0.12\,\mathrm{km}$ compared to the simulation ABL height. The ABL height derived from the dropsondes was $0.07\,\mathrm{km}$ at C01, $0.43\,\mathrm{km}$ at C02, and $1.04\,\mathrm{km}$ at C03, resulting in an overall root mean square error (RMSE) of $0.14\,\mathrm{km}$ compared to the simulation. The conclusion from this evaluation against the three datasets is that the model reproduces the observed ABL height within $150\,\mathrm{m}$ throughout the simulation. The temporarily reduced deepening rate between C02 and C03 in the simulation is supported by the measured data, which is an interesting feature that could be related to the low-level maximum in subsidence during that period (Figure 4a).

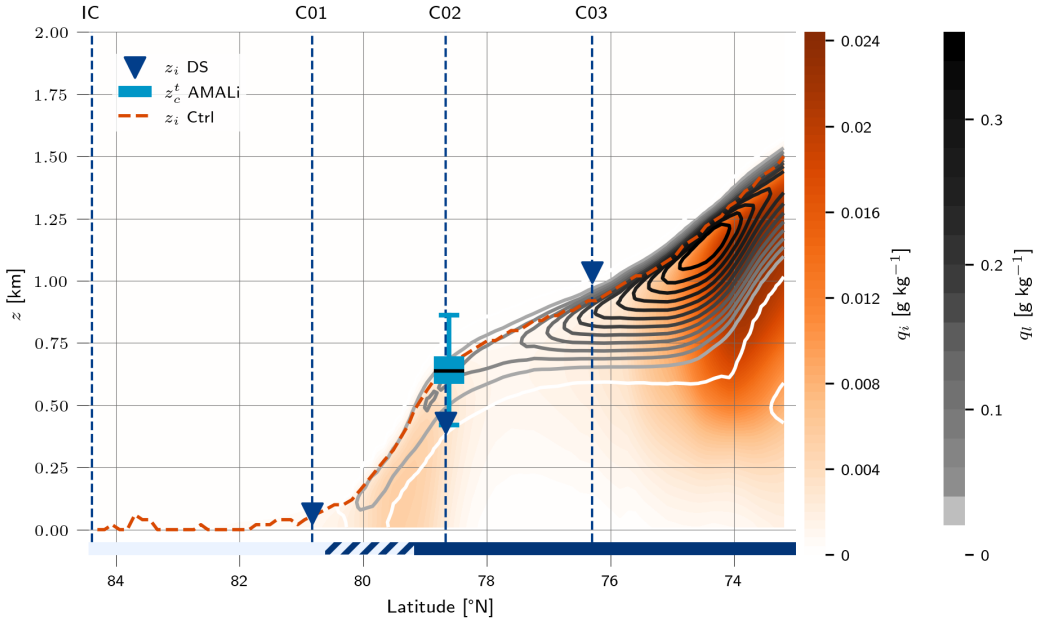

Figure 5. Latitudinal evolution of cloud liquid (grey contour lines) and ice (red filled contours) along the MCAO trajectory. Results from the $45\,\mathrm{h}$ semi-Lagrangian DALES simulation Ctrl are shown, including model ABL height (red dashed), compared to dropsonde ABL heights (▼) and cloud-top heights from AMALi lidar aboard the P5 aircraft (light blue boxplot, outliers not shown for better visibility). Dashed vertical lines indicate dropsonde circle locations.

4.2 Temperature and humidity profiles

The vertical structure of virtual potential temperature (ϑ_v) and specific humidity (q) in the Ctrl experiment is evaluated against in-situ observations from HALO dropsondes, closest to the simulation trajectory; the variability of all soundings in each circle is

https://doi.org/10.5194/egusphere-2026-554
Preprint. Discussion started: 11 February 2026

indicated as blue shading in Figure 6. This comparison reveals possible systematic biases in the thermodynamic state. Figure 6 focuses on the lowest 3 km of the atmosphere to highlight the ABL properties. Above 3 km altitude, the simulation matches the observations of ϑ_v with an agreement of more than 99 % (Equation (C2)) at all three locations, following a logarithmic profile. Profiles of q above 3 km are reproduced with an agreement of more than 67 % at C01, C02 and C03, with the larger differences resulting from observed humidity layers not captured in the smoother simulated humidity structure.

In the region of C01 (Figure 6 (a) and (d)), located above sea ice near its edge, an inversion in ϑ_v is detected near the surface at 30 m in the simulation, and at 20 m in the dropsonde profiles, with a thermodynamic wind profile above it. The simulated near surface values of ϑ_v of $-25.6\,^{\circ}\mathrm{C}$ agree within the standard deviation with the dropsonde observations with a measured value of $-24.2\,^{\circ}\mathrm{C}$. The general agreement of the temperature profiles below 3 km is 99.7 %. In contrast, the measured humidity profiles exhibit a larger spread among the sondes; however, the closest profile agrees well with the slightly smoother simulated profile, indicating good overall consistency. In contrast, the humidity profiles differ in their variability, as the dropsondes resolve several humid layers that are not captured by the modelled profile. The near-surface value of q at C01 was $0.5\,\mathrm{g\,kg^{-1}}$ in the simulation and $0.54\,\mathrm{g\,kg^{-1}}$ in the observations, and the overall profiles agree by 81 % below 3 km. The good agreement at C01 reflects the continuous nudging that is active above the ABL top, which is still very low at this stage.

As the air mass moved over the marginal sea ice zone (MIZ) and the open ocean to the location of C02 (Figure 6 (b) and (e)), surface warming caused an increase in the near surface air temperature $\vartheta_{v,0}$ in the simulation of $+14.5\,\mathrm{K}$ to $-11.1\,^{\circ}\mathrm{C}$, while observed warming was even stronger with a measured increase in $\vartheta_{v,0}$ of $+15.6\,\mathrm{K}$ to $-8.6\,^{\circ}\mathrm{C}$. The inversion height was approximately 590 m in both profiles, but the simulated inversion was less steep. The profile below the inversion shows a cold deviation of 3.3 K, but the shape of the curve matches the measured profile, corresponding to an agreement of 98 % below the thermal inversion. The increase in evaporation over the open ocean led to an increase in humidity with surface moisture q_0 of $1.5\,\mathrm{g\,kg^{-1}}$ in the simulation and $1.6\,\mathrm{g\,kg^{-1}}$ in the observations. Both show a pronounced drop in humidity near 590 m, with the observed jump being stronger and sharper than the simulation, induced by the prescribed advection of q_t (shown in Figure 4c). Within the mixed layer, where temperature and humidity are uniform with height, the model underestimates the humidity by an average of $0.2\,\mathrm{g\,kg^{-1}}$ with an agreement of 88 % below the temperature inversion. Due to observed moisture layers above the temperature inversion, which did not appear in the simulation, the agreement in the overall profile of q is 82 % below 3 km.

Further south, over the open ocean at C03 (Figure 6 (c) and (f)), the ABL has deepened further and ϑ_v has continued to increase, with a simulated surface value of $\vartheta_{v,0}$ of $-7.5\,^{\circ}\mathrm{C}$ and an observed value of $-4.6\,^{\circ}\mathrm{C}$ representing an underestimation of near-surface warming by 2.9 K. The modelled inversion base is at 830 m, compared to 1000 m in the observations, with the simulated inversion being less steep. Below the temperature inversion, the model underestimates ϑ_v by approximately 2 K although the agreement of the entire shown profile is still 99.6 %. Therefore, there is a consistent cold bias of $-2\,\mathrm{K}$ to $-3\,\mathrm{K}$ across all circles, a tendency also found by (Wendisch et al., 2025) in the limited-area configuration of the ICON model for all observed MCAO cases of HALO–$(\mathcal{AC})^3$. The humidity in the boundary layer at C03 has also increased further, reaching $1.7\,\mathrm{g\,kg^{-1}}$ in the simulation and $2\,\mathrm{g\,kg^{-1}}$ in the observations, with the model underestimating the surface layer of strong humidity directly above the ocean. Also, in humidity, the simulated jump is weaker. Below the temperature inversion, the model underestimates q by $0.2\,\mathrm{g\,kg^{-1}}$, which corresponds to an agreement of 90 % below, while above the inversion,

https://doi.org/10.5194/egusphere-2026-554
Preprint. Discussion started: 11 February 2026

the absence of observed moisture layers reduces the agreement to 33 %. A consistent moisture deviation of $-0.15\,\mathrm{g\,kg^{-1}}$ to $-0.22\,\mathrm{g\,kg^{-1}}$ was found in all three profiles.

Additional measurements taken with the CMET sonde drifting south along a similar trajectory further support these results. At the same latitude as C01, the CMET flew at an altitude of $340\,\mathrm{m}$ at a distance of $225\,\mathrm{km}$ to the simulated trajectory. The CMET reached the latitude of interest about $2.5\,\mathrm{h}$ later than the simulated air parcel. Here, $\vartheta_v = -8.8\,^\circ\mathrm{C}$ and $q = 0.52\,\mathrm{g\,kg^{-1}}$ were measured, which largely corresponds to the simulation in terms of humidity (difference of only $0.02\,\mathrm{g\,kg^{-1}}$), but with ϑ_v being $5.7\,\mathrm{K}$ warmer, which may be due to the proximity to Svalbard and the associated local warming effects. As the trajectory of CMET was closer to Svalbard and travelled through the cloud-free region associated with lee-effects, likely causing a warming of the lower layers. The CMET reached the latitude of C02 $7.5\,\mathrm{h}$ later at a distance of $132\,\mathrm{km}$ from the simulated trajectory. The CMET measured at $902\,\mathrm{m}$ above sea level a temperature of $\vartheta_v = -1.8\,^\circ\mathrm{C}$ and $q = 0.25\,\mathrm{g\,kg^{-1}}$, which is $3.7\,\mathrm{K}$ warmer and $0.2\,\mathrm{g\,kg^{-1}}$ drier than the simulation. At C03, the CMET was $2\,\mathrm{h}$ later and $149\,\mathrm{km}$ away from the simulation at an altitude of $1780\,\mathrm{m}$. A virtual potential temperature ϑ_v of $2.7\,^\circ\mathrm{C}$ was measured, $1.8\,\mathrm{K}$ warmer than in the model and $q = 0.78\,\mathrm{g\,kg^{-1}}$, only $0.06\,\mathrm{g\,kg^{-1}}$ more humid. As the CMET moved south and the influence of Svalbard diminished, the measured air mass increasingly resembled that observed by the dropsondes, with the humidity in all three circles corresponding very closely to the simulated q values measured by the dropsondes.

The overall conclusion from these results is that the LES model reproduces the observed evolution in the vertical thermodynamic structure after C01 to a reasonable degree. This is not trivial, as the nudging takes place above the temperature inversion only, and below it, the simulated ABL is free to evolve. A slight cold and dry bias is evident within the ABL, and the inversions at its top height appear less pronounced than observed. These differences may arise from (i) uncertainties in the surface boundary condition T_{skin}, and (ii) shortcomings in the bulk flux parametrisation at the surface. Nevertheless, the overall correspondence between simulation and observation indicates that the model adequately reproduces the thermodynamic structure of the observed MCAO, providing a robust basis for further analysis.

4.3 Integrated water paths

The model performance in representing various column-integrated quantities is assessed next. In Figure 7 (a), the simulated integrated water vapour (IWV) is evaluated against observations from two sources. The first source are the data from the HAMP radiometer on board HALO which measured along the flight trajectory, and the second is the IWV determined from the dropsonde humidity profiles, averaged over the ten sondes in each circular pattern. The simulation accurately replicated the observed IWV at C01 of $1.9\,\mathrm{kg\,m^{-2}}$ with a small difference of $0.1\,\mathrm{kg\,m^{-2}}$. At C02, the dropsondes measured $2.7\,\mathrm{kg\,m^{-2}}$ IWV, reproduced with $+0.04\,\mathrm{kg\,m^{-2}}$ in the simulation. At C03, the observed IWV was $4.4\,\mathrm{kg\,m^{-2}}$, which the simulation was slightly overestimated by $+0.3\,\mathrm{kg\,m^{-2}}$. This temporal evolution of IWV closely follows the HAMP observations, with an RMSE of $0.2\,\mathrm{kg\,m^{-2}}$ compared to the simulation. These results suggest that the net input of humidity into the deepening ABL is well captured by the model.

Figure 7 (b) compares the simulated liquid water path LWP against two measurements. The LWP retrieved from HAMP onboard HALO exhibits a much higher short-term variability than in the simulation, resulting in an RMSE of $30\,\mathrm{g\,m^{-2}}$. Despite

https://doi.org/10.5194/egusphere-2026-554
Preprint. Discussion started: 11 February 2026

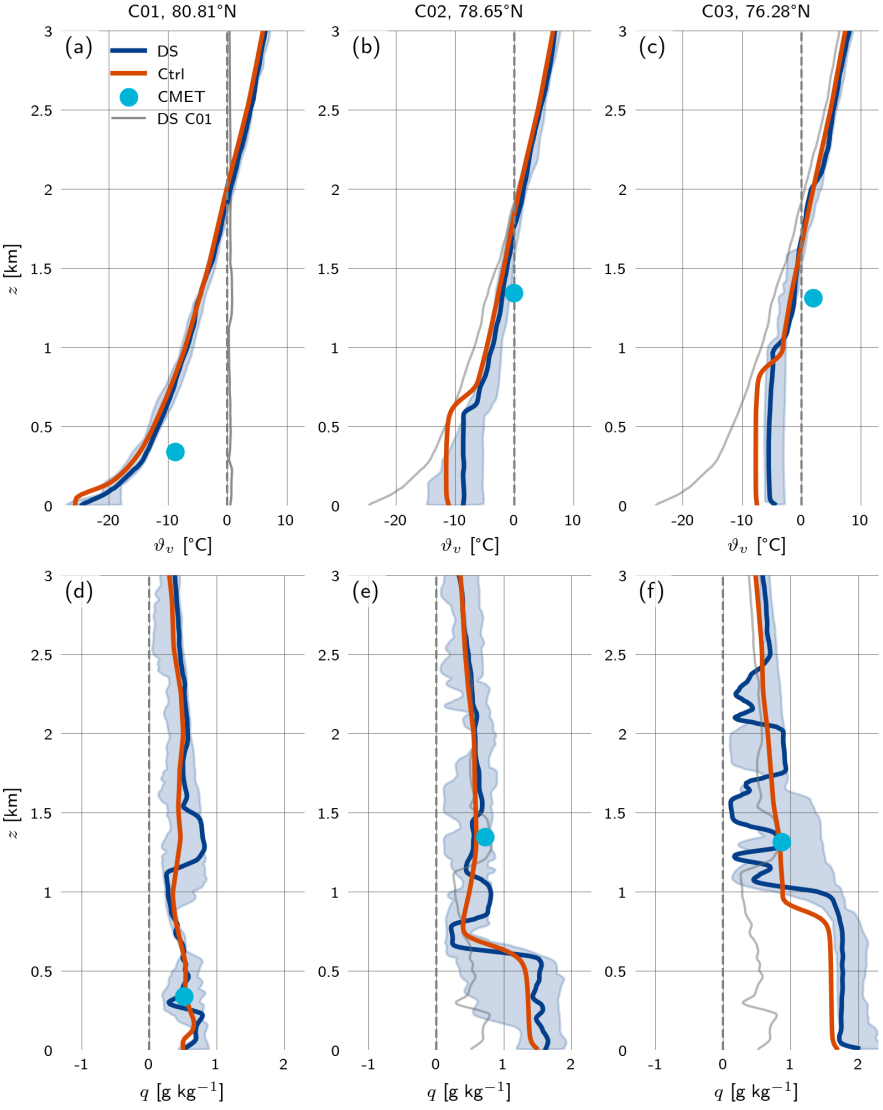

Figure 6. Vertical profiles of virtual potential temperature (ϑ_v) and specific humidity (q). Dropsonde profile (blue) of the dropsonde closest to the simulation trajectory and spread between values measured by 10 sondes per circle (shading); simulation profiles are shown in red. CMET measurements are indicated as blue dots.

https://doi.org/10.5194/egusphere-2026-554
Preprint. Discussion started: 11 February 2026

this, the overall temporal evolution aligns with the simulated LWP, with liquid water appearing as soon as the MIZ is reached. The MiRAC instrument on P5 showed even higher variability due to its high spatial resolution and low flight altitude above the clouds. When averaged, MiRAC observations yield a mean LWP of $0.01\,\mathrm{g\,m^{-2}}$, which appears much lower than the simulated LWP of $12\,\mathrm{g\,m^{-2}}$, but the simulation value lies within the spread of the LWP observed by MiRAC. These results suggest that, while the observed LWP fluctuates more strongly due to higher resolution, capturing individual cloud streets, than the smoother, domain-average model output, the simulation captures the general trend and magnitude of the evolution of liquid water throughout the event.

The simulated ice water path of all frozen hydrometeors IWP shown in Figure 7 (c) is only compared to MiRAC measurements aboard P5. The IWP retrievals by HALO were excluded due to large uncertainties for this case. The average observed IWP from MiRAC was $0.6\,\mathrm{g\,m^{-2}}$, but similar to the LWP observations, the variability due to the high resolution of individual clouds is large and values range up to $6.2\,\mathrm{g\,m^{-2}}$. This high variability may also result from the substantial uncertainties associated with IWP retrievals. The Ze–IWC relationship of (Hogan et al., 2006) exhibits uncertainties around a factor of 2, caused by the strong temperature dependence of ice particle size distributions and densities. At warmer temperatures, the ice water content IWC tends to be overestimated, whereas at colder temperatures it is generally underestimated. This temperature sensitivity is particularly relevant for 94 GHz radar, where Mie-scattering further increases the retrieval uncertainty. Compared to the simulated IWP in the location of the P5 measurements of $2.58\,\mathrm{g\,m^{-2}}$, an RMSE of $73.34\,\mathrm{g\,m^{-2}}$ is found. It should also be noted that the P5 observations do not coincide with the air mass trajectory but were collected at a later time, limiting the comparability of the data (Figure 1). A notable feature of the latitudinal evolution of the simulated IWP is the local maximum reached in the simulation just before C02; the realism cannot be verified due to the absence of reliable IWP measurements along the whole trajectory.

4.4 Surface heat fluxes

The surface heat fluxes are key drivers of ABL evolution in MCAOs. To evaluate the simulated sensible (H) and latent (E) heat fluxes, we estimate these data from dropsonde observations following the thermodynamic method suggested by Hartmann et al. (1997). This method assumes steady-state conditions, negligible radiative divergence and cross-flow advection, and minimal entrainment above the mixed layer. Then, the sensible and latent heat energy fluxes can be calculated as

$$H_{\mathrm{DS}} = \varrho \cdot c_p \cdot u_{\mathrm{ML}} \int_{z_i}^{0} \frac{\Delta\vartheta}{-\Delta y}\,\mathrm{d}z - H_{\mathrm{C}}, \tag{6}$$

$$E_{\mathrm{DS}} = \varrho \cdot L_v \cdot u_{\mathrm{ML}} \int_{z_i}^{0} \frac{\Delta q}{-\Delta y}\,\mathrm{d}z + H_{\mathrm{C}}, \tag{7}$$

where ϱ represents the air density, c_p the specific heat capacity, L_v the latent heat of evaporation, u_{ML} the mean horizontal wind speed within the mixed layer and z_i the height of the ABL. Δy is the horizontal distance between two profiles. The

https://doi.org/10.5194/egusphere-2026-554
Preprint. Discussion started: 11 February 2026

contribution of condensational heating within the cloud layer is represented by the following formulas:

$$H_C = \varrho \cdot L_v \cdot u_{\mathrm{ML}} \int_{z_i}^{z_c^b} \frac{\Delta l}{-\Delta y}\,\mathrm{d}z, \tag{8}$$

where z_b represents the height of the cloud base, defined as the lowest altitude at which the relative humidity reaches saturation with respect to the ice or liquid. Meanwhile, Δl refers to the difference in q_l between the profiles, which is approximated as the upper limit of q_l within the cloud layer. This is estimated as the difference of q_t within the cloud and the average $\overline{q_{t,\mathrm{BC}}}$ below the cloud layer, following (Hartmann et al., 1997). In the model, the surface heat fluxes can be sampled continuously as

$$H_{\mathrm{Ctrl}} = \varrho \cdot c_p \cdot \overline{w' \cdot \vartheta'}, \tag{9}$$

$$E_{\mathrm{Ctrl}} = \varrho \cdot L_v \cdot \overline{w' \cdot q'}, \tag{10}$$

with $\overline{w'\vartheta'}$ and $\overline{w'q'}$ representing the turbulent kinematic fluxes of temperature and moisture at the surface.

The simulation produced H_{Ctrl} values up to $830\,\mathrm{W\,m^{-2}}$ and E_{Ctrl} values up to $102\,\mathrm{W\,m^{-2}}$ over the open ocean. In particular, the sensible heat flux is substantially higher than the climatological mean sensible flux of about $200\,\mathrm{W\,m^{-2}}$ during MCAOs, while the latent heat flux is comparable to the climatological mean latent heat flux of $100\,\mathrm{W\,m^{-2}}$ reported by Papritz and Spengler (2017) for MCAOs in the region west of Svalbard. The difference in potential temperature between the near-surface atmosphere and the ocean surface causes a direct response in the sensible heat flux, while the latent heat flux is limited by the saturation specific humidity at the sea surface temperature (Papritz et al., 2015; Papritz and Spengler, 2017). In the observed region, H was generally more efficient than E in extracting energy from the ocean surface, but the relative importance of E increased as the air is mass advected away from the sea-ice edge over warmer waters. South of 75 °N, the mean values of H_{Ctrl} and E_{Ctrl} were $69\,\mathrm{W\,m^{-2}}$ and $17\,\mathrm{W\,m^{-2}}$, respectively, consistent with the findings of Brümmer (1997).

Dropsonde-derived H_{DS} values considerably underestimate simulated surface sensible heat fluxes by $564\,\mathrm{W\,m^{-2}}$ between C01 and C02 and $306\,\mathrm{W\,m^{-2}}$ between C02 and C03. We speculate that this offset is mostly due to numerous assumptions in the method of deriving them from observed profiles. To improve comparability between model and measurements and gain insight, the same diagnostic technique is now applied to the simulated profiles (Figure 6), which yields much better agreement. The associated RMSE is $95\,\mathrm{W\,m^{-2}}$ between H_{DS} and $H_{\mathrm{Ctrl,\,Prof}}$, due to a large underestimation of $H_{\mathrm{Ctrl,\,Prof}}$ between C02 and C03 of only $21\,\mathrm{W\,m^{-2}}$, while $H_{\mathrm{DS}} = 170\,\mathrm{W\,m^{-2}}$. Note that the dropsonde-derived E_{DS} in the marginal ice zone (C01–C02) is very small ($2.6\,\mathrm{W\,m^{-2}}$) compared to the simulated fluxes that exceeded $100\,\mathrm{W\,m^{-2}}$, but increased to $16\,\mathrm{W\,m^{-2}}$ between C02 and C03, closer to the simulated values. The RMSE of $8.9\,\mathrm{W\,m^{-2}}$ between E_{DS} and $E_{\mathrm{Ctrl,\,Prof}}$ indicates that although the observational profile-based method struggles to fully capture the true flux magnitudes in the early MCAO phase, it reproduces their relative variability well when applied consistently.

5 Results II: Subsidence impacts

The results discussed so far indicate that the Ctrl simulation reproduces the temporal evolution of the ABL well, including various water paths and surface energy fluxes. Therefore, the Ctrl experiment represents a robust and realistic foundation for

https://doi.org/10.5194/egusphere-2026-554
Preprint. Discussion started: 11 February 2026

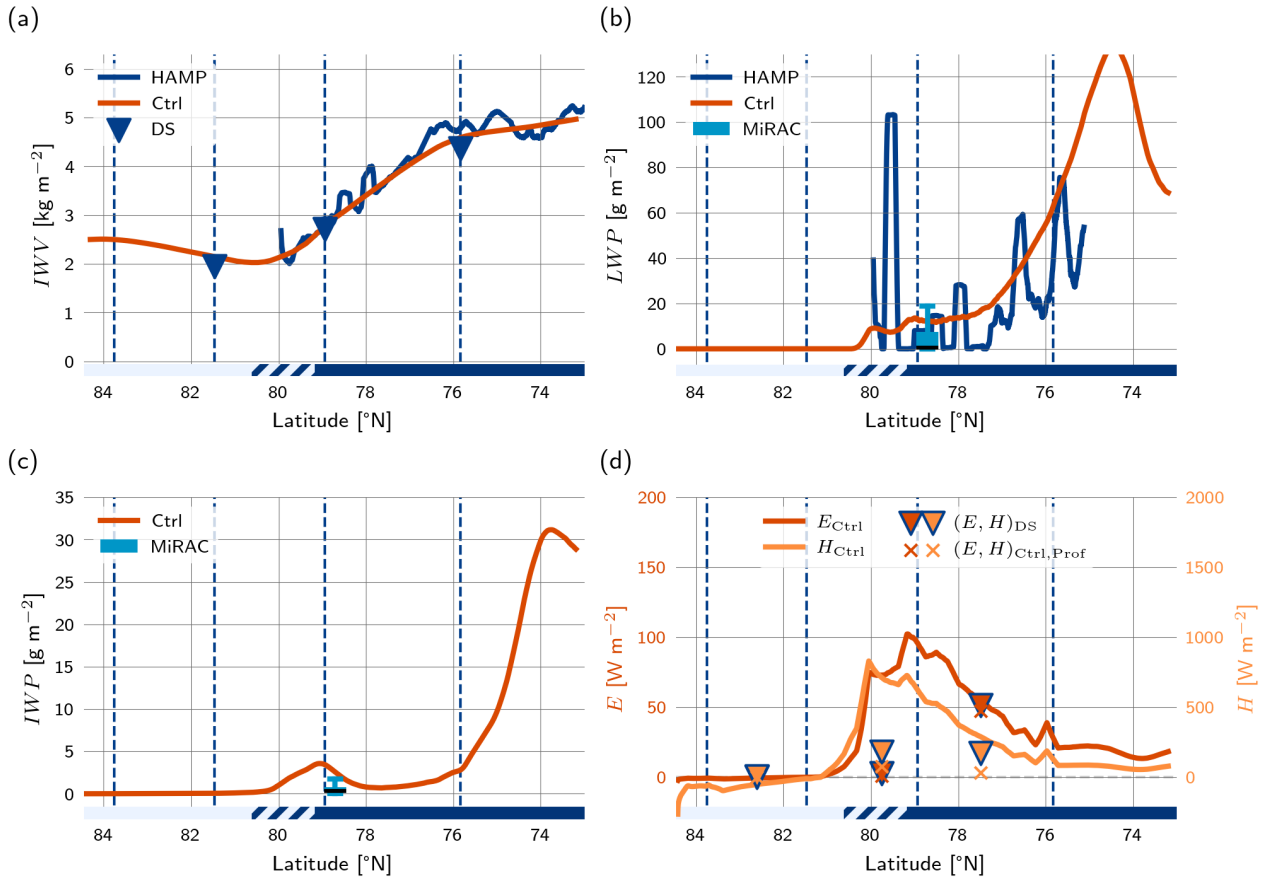

Figure 7. Latitudinal evolution of various bulk properties of the simulated MCAO in the Ctrl experiment. (a) Integrated water vapour IWV simulation (red line) compared to longitudinally averaged observations from HALO (blue line) and estimates based on dropsonde data (▼). (b) Simulated liquid water path LWP and (c) ice water path IWP (red lines) compared to HALO (dark blue line) and P5 (light blue boxplot, outliers not shown for better visibility) observations. (d) Simulated surface latent (E, red line) and sensible (H, yellow line) heat fluxes compared to estimates based on dropsonde data following the method of Hartmann et al. (1997) (▼). The same method applied to model profiles is also shown, for reference (×). In all figures, the vertical dashed lines mark the location of the dropsonde circles. The coloured bar at the bottom indicates sea ice ($sic > 0.9$, light blue), marginal sea-ice ($0 < sic \leq 0.9$, hatched), and open ocean ($sic = 0$, dark blue).

https://doi.org/10.5194/egusphere-2026-554
Preprint. Discussion started: 11 February 2026

subsequent Lagrangian LES sensitivity experiments, as applied in this section to investigate the impact of mesoscale subsidence on the ABL and cloud evolution. In total, five experiments with differing mesoscale subsidence are performed and analysed. As described in Section 3.4, four additional experiments were conducted with the Ctrl subsidence field multiplied by a factor $\{0,\ 0.1,\ 0.5,\ 2.0\}$, respectively.

5.1 Sensitivity analysis

Figure 8 shows the evolution of q_l and q_i along the MCAO trajectory. In the no-subsidence (NoSub) setup, the cloudy ABL deepens the fastest, approaching a parabolic deepening rate ($\sim t^{1/2}$) after the air mass moves over the open ocean (Stevens, 2007). In this setup, the cloud mass is the largest, both in liquid and frozen form. The higher the prescribed subsidence forcing, the more the ABL deepening driven by turbulent/convective entrainment is suppressed by subsidence. This in particular applies during the time period between C02 and C03, where the observed low-level subsidence has its maximum (Figure 4a). This leads to the development of thinner clouds and less q_l and q_i. In the Sub200 case, only a very thin, shallow mixed-phase cloud is observed.

To gain more insight into the spatial structure of the cloud field, Figure 9 presents horizontal cross-sections of q_l and q_i through the centre of the simulated domain for all five simulations. These locations are sampled at regular intervals along the trajectory, beginning at C01 near the sea-ice edge and extending southward to $73.25\,^{\circ}\mathrm{N}$ at the end of the simulation period. The grey shading highlights regions in which the cloud layer is decoupled from the surface, following the criterion of Jones et al. (2011). This diagnostic is defined by the thresholds $\Delta q_t = \overline{q}_{t,\mathrm{bot}} - \overline{q}_{t,\mathrm{top}} > 0.5\,\mathrm{g\,kg^{-1}}$, based on the layer-mean total-water mixing ratio in the upper and lower $25\,\%$ of the boundary layer, and $\Delta\vartheta_l = \overline{\vartheta}_{l,\mathrm{top}} - \overline{\vartheta}_{l,\mathrm{bot}} > 0.5\,\mathrm{K}$, calculated analogously for the layer-mean liquid-water potential temperature. These metrics have been associated with the onset of boundary-layer decoupling and the subsequent transition from roll convection to open-cell structures in MCAOs (Karalis et al., 2022; Abel et al., 2017). What stands out during the decoupled phase is the presence of liquid-phase shallow cumulus clouds, rising into the capping mixed-phase cloud layer.

Across the simulations, the onset of decoupling exhibits a systematic dependence on the prescribed subsidence: in cases with reduced subsidence, the decoupling occurs closer to the sea-ice edge and is accompanied by overall larger maxima in both liquid and ice water content. While all simulations show the initial formation of a thin ice cloud at C01, substantial differences arise beginning at C02, most notably in cloud-top height and the vertical distribution of liquid and ice. The Sub200 simulation produces only a shallow ice cloud capped by a thin liquid layer, with little variation in cloud-top altitude throughout the trajectory. In contrast, the simulations with weaker subsidence develop considerably deeper clouds, characterised by more complex internal structure and enhanced condensate mass.

The impact of subsidence on the developing ABL is characterised by various bulk quantities, as shown in Figure 10. The integrated water vapour IWV (Figure 10 (a)) is similar in all simulations, but the boundary layer (Figure 10 (d)) in the NoSub case reaches substantially greater depths ($2\,\mathrm{km}$), following a parabolic deepening rate due to unimpeded entrainment at the ABL top. All simulations exhibit a similar strong initial boundary layer growth within the MIZ and immediately downstream of the sea ice edge (up to C02), driven primarily by intense surface heat fluxes in this region (Figure 7). However, after this

https://doi.org/10.5194/egusphere-2026-554
Preprint. Discussion started: 11 February 2026

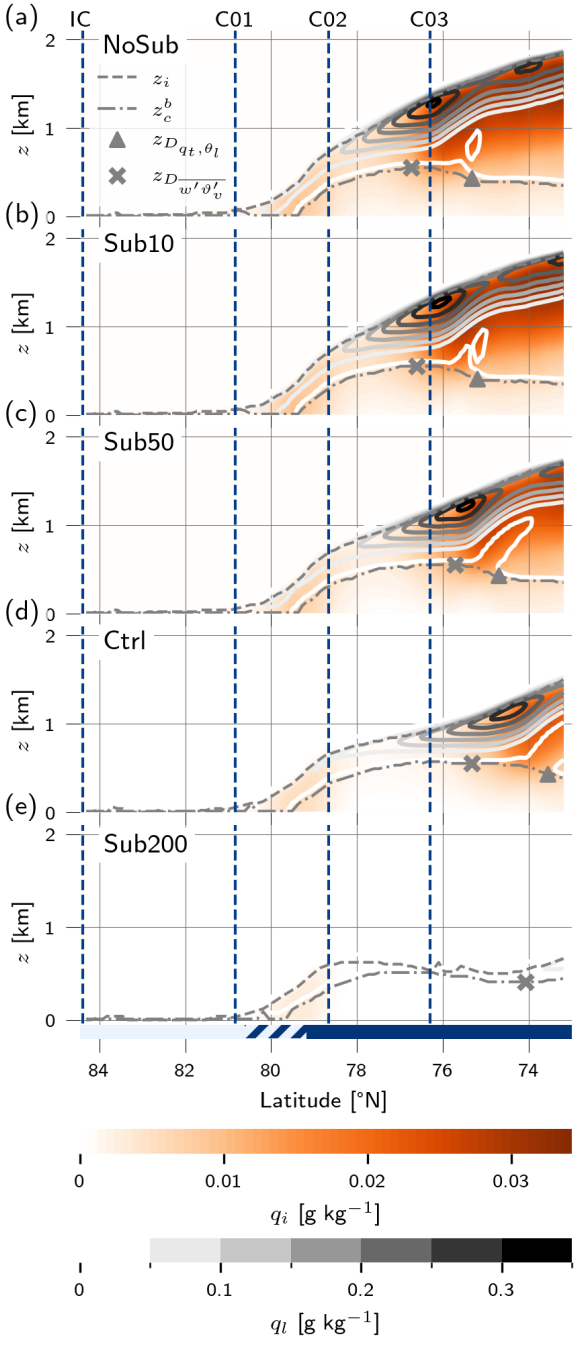

Figure 8. Latitudinal evolution of cloud liquid (grey) and ice (red) along the MCAO trajectory for all sensitivity experiments. Dashed horizontal lines indicate dropsonde circle locations. Boundary layer height z_i and cloud base z_c^b are indicated by grey dashed and dot-dashed lines, respectively. The markers $\times$ and ▼ indicate decoupling points and heights with respect to $\overline{w'\vartheta_v'}$ and Δq_t and $\Delta\vartheta_l$ respectively (Section 5.2 for definition). The coloured bar at the bottom indicates sea ice ($sic > 0.9$, light blue), marginal sea-ice ($0 < sic \leq 0.9$, hatched), and open ocean ($sic = 0$, dark blue).

https://doi.org/10.5194/egusphere-2026-554
Preprint. Discussion started: 11 February 2026

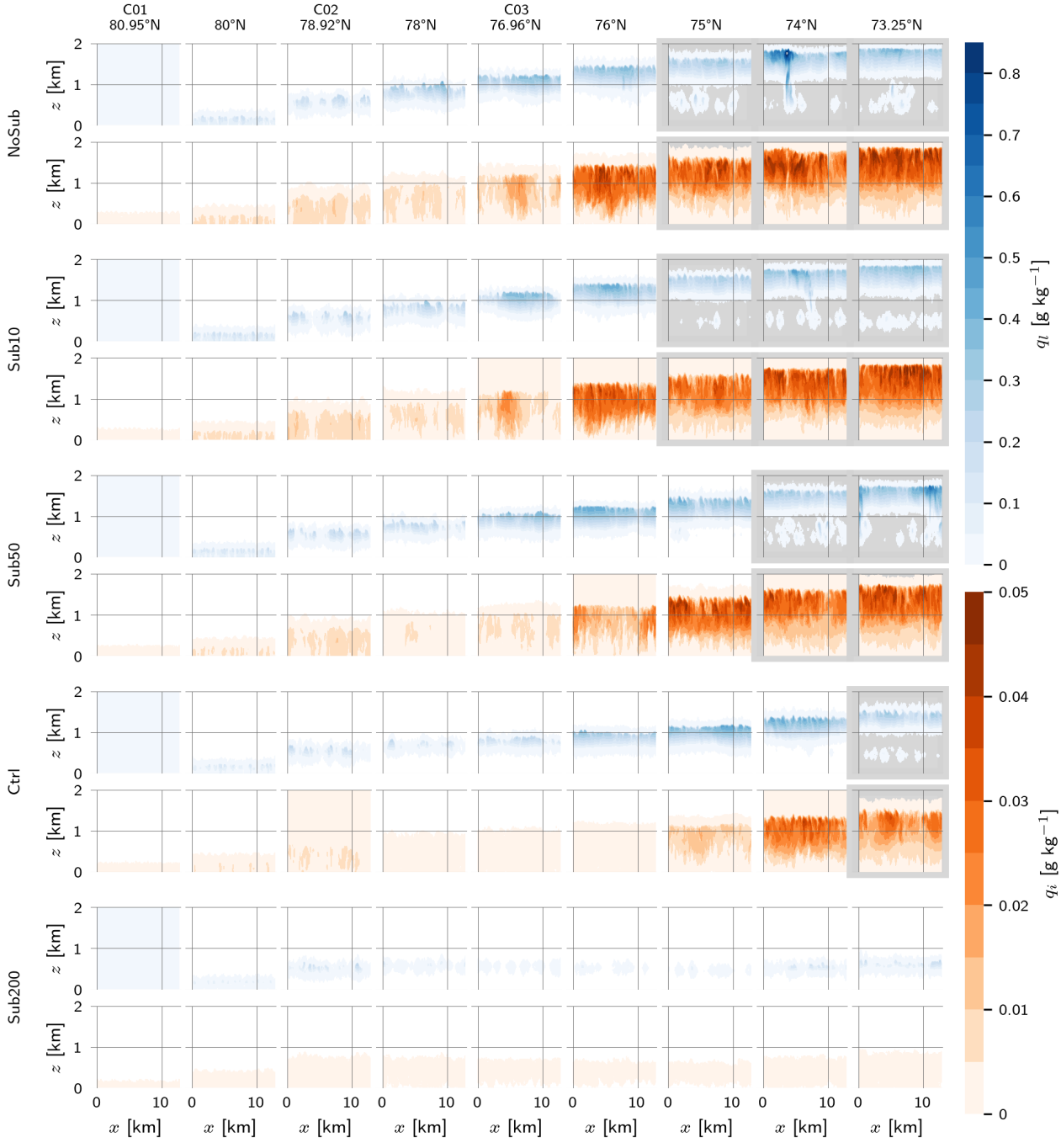

Figure 9. Horizontal cross-sections of cloud liquid water (q_l) and cloud ice (q_i) at the domain centre ($y = 6.4\,\mathrm{km}$), at different locations along the trajectory and for different subsidence experiments. Cross-sections of decoupled clouds ($\Delta q_t > 0.5\,\mathrm{g\,kg^{-1}}$ and $\Delta \vartheta_l > 0.5\,\mathrm{K}$) are highlighted in grey.

https://doi.org/10.5194/egusphere-2026-554
Preprint. Discussion started: 11 February 2026

initial phase, the Sub200 simulation boundary layer actually becomes shallower, with the strong subsidence keeping z_i below $1\,\mathrm{km}$. In contrast, the Ctrl, Sub50, and Sub10 simulations all maintain continued ABL deepening, though z_i remains below the parabolic limit visible in NoSub.

The liquid water path LWP (Figure 10 (c)) exhibits an initial peak near the sea ice in all simulations, coinciding with the region of strong boundary layer growth at approximately $80\,^{\circ}\mathrm{N}$ on average. The RMSE in the location of the peak between the simulations is $0.01\,^{\circ}\mathrm{N}$, and the strength of the peak decreases with increasing subsidence by $18\,\mathrm{g\,m^{-2}}$, with an overall RMSE of $4.9\,\mathrm{g\,m^{-2}}$. A second, more pronounced LWP maximum occurs later at $76.3\,^{\circ}\mathrm{N}$ in NoSub, with a maximum value of $173\,\mathrm{g\,m^{-2}}$. For Sub50 and Ctrl, this secondary peak shifts to lower latitudes and reduced magnitudes, occurring at $76\,^{\circ}\mathrm{N}$ ($167\,\mathrm{g\,m^{-2}}$) and $74.4\,^{\circ}\mathrm{N}$ ($133\,\mathrm{g\,m^{-2}}$), respectively. In Sub200, the liquid water path does not recover after the initial maximum and shows only a gradual increase later in the simulation, beyond $74\,^{\circ}\mathrm{N}$.

The ice water path IWP (Figure 10 (e)), including all frozen hydrometeors, displays a similar spatial evolution, with an initial peak forming in the MIZ around $79.4\,^{\circ}\mathrm{N}$, consistent in all simulations. Subsequently, IWP increases over the open ocean following the sea ice edge. Compared to LWP the ice growth begins slightly earlier (also visible in Figure 9), which is consistent with previous studies of Arctic MCAOs (Murray-Watson and Gryspeerdt, 2024; Inoue et al., 2021). The peak IWP in NoSub occurs at $75.7\,^{\circ}\mathrm{N}$ with $48\,\mathrm{g\,m^{-2}}$, whereas for Sub50 and Ctrl it shifts to $75.7\,^{\circ}\mathrm{N}$ and $73.8\,^{\circ}\mathrm{N}$ respectively with reduced magnitudes of $41\,\mathrm{g\,m^{-2}}$ and $31\,\mathrm{g\,m^{-2}}$ respectively. The Sub200 simulation exhibits no such shift or comparable peak values, indicating a systematic suppression of ice growth under stronger subsidence.

The ratio of ice to liquid water, $\frac{IWP}{LWP}$, calculated only for regions with a significant liquid content ($LWP > 1\,\mathrm{g\,m^{-2}}$), highlights these differences more clearly (Figure 10 (b)). The initial shallow cloud developing above the MIZ shows a similar structure among NoSub, Sub10, Sub50, and Ctrl, while Sub200 displays a slightly larger ice fraction in the initial cloud. However, because of the overall thinness of both liquid and ice layers, this difference cannot be regarded statistically significant. In later stages, LWP in Sub200 falls below $1\,\mathrm{g\,m^{-2}}$, producing a discontinuity in the $\frac{IWP}{LWP}$ ratio, while in the remaining cases a clear shift toward later growth of IWP is evident.

Finally, the impact of subsidence on the total surface precipitation rate (P_{tot}) (Figure 10 (f)) is broadly similar to the IWP. The NoSub simulation reaches precipitation rates up to $60\,\mathrm{mm\,h^{-1}}$ toward the end of the simulation, compared with $25\,\mathrm{mm\,h^{-1}}$ at the peak near $74\,^{\circ}\mathrm{N}$ for Ctrl. In Sub200, precipitation remains confined to the initial shallow cloud phase, with maximum rates of only $2.1\,\mathrm{mm\,h^{-1}}$.

5.2 Glaciation and decoupling

The results so far indicate that the behaviour of the cloud ice phase is particularly affected by the strength of subsidence. To gain further insight, the relative contributions by the three frozen hydrometeor classes in the LES microphysical scheme are investigated. The integrated column water paths of cloud ice ($CIWP$), snow ($SIWP$), and graupel ($GIWP$) are shown in Figure 11. The behaviour of $CIWP$ (Figure 11 (a)) closely follows that of the total ice water path (IWP), reflecting its dominant contribution to the total ice mass. The maximum values of $CIWP$ reach $38\,\mathrm{g\,m^{-2}}$ at $73.4\,^{\circ}\mathrm{N}$ for NoSub and $32\,\mathrm{g\,m^{-2}}$ at $73.7\,^{\circ}\mathrm{N}$ for Ctrl, with a systematic decrease in amplitude under stronger subsidence. The $SIWP$ (Figure 11 (c))

https://doi.org/10.5194/egusphere-2026-554
Preprint. Discussion started: 11 February 2026

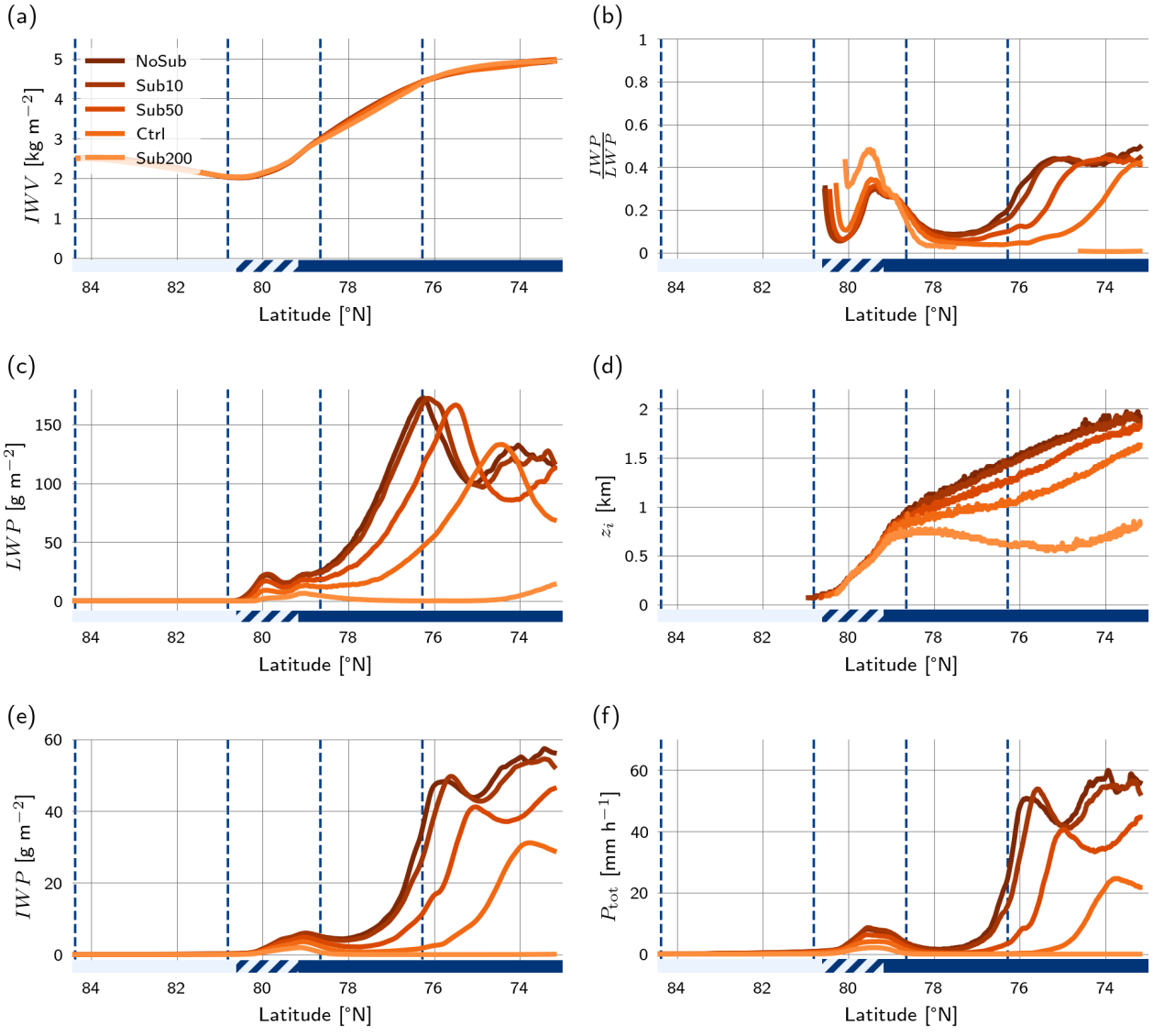

Figure 10. Integrated water vapour IWV (a), liquid water path LWP (c), ice water path IWP (e), including all frozen hydrometeors, together with its ratio $\frac{IWP}{LWP}$ (b), the boundary layer height z_i (d) and the total precipitation rate P_{tot} (e) for Lagrangian LES with different subsidence forcings. The locations of the dropsonde circles are shown as vertical dashed lines, and the surface cover is indicated as sea ice ($sic > 0.9$, light blue), marginal sea-ice zone ($0 < sic \leq 0.9$, hatched), and open ocean ($sic = 0$, dark blue).

https://doi.org/10.5194/egusphere-2026-554
Preprint. Discussion started: 11 February 2026

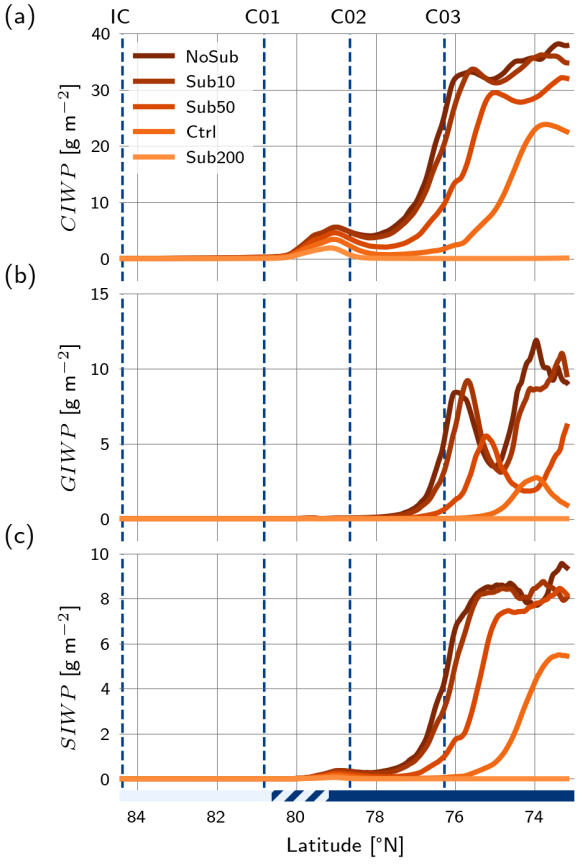

Figure 11. Integrated cloud ice water path $CIWP$ (a), integrated snow water path $SIWP$ (c) and integrated graupel water path $GIWP$ (b). The locations of the dropsonde circles are shown as vertical dashed lines, and the surface cover is indicated as sea ice ($sic > 0.9$, light blue), marginal sea-ice zone ($0 < sic \leq 0.9$, hatched), and open ocean ($sic = 0$, dark blue).

distribution exhibits a similar latitudinal progression, with peak values occurring later and at reduced magnitudes as subsidence increases. However, unlike $CIWP$, $SIWP$ does not sharply decline after the peak but plateaus afterwards, reaching $9.6\,\mathrm{g\,m^{-2}}$ at $73.3\,^{\circ}\mathrm{N}$ for NoSub and $5.5\,\mathrm{g\,m^{-2}}$ at $73.4\,^{\circ}\mathrm{N}$ for Ctrl. The graupel path $GIWP$ (Figure 11 (b)) exhibits the most distinct and localised peak. In NoSub the peak occurs at $76\,^{\circ}\mathrm{N}$ with a magnitude of $8.4\,\mathrm{g\,m^{-2}}$, generally shifting southward with increasing subsidence to $74\,^{\circ}\mathrm{N}$ for Ctrl, weakening in amplitude to $2.7\,\mathrm{g\,m^{-2}}$. The Sub200 experiment does not develop graupel. In this southward progression, the width of the graupel peak remains similar.

Graupel is typically formed in convective updrafts, as it requires substantial vertical velocities. Accordingly, the southward shift and progressive weakening of the peak in $GIWP$ with increasing subsidence probably reflects a similar shift in convective dynamics. This motivates a deeper investigation of the behaviour of boundary-layer internal decoupling. Previous MCAOs studies have established that such decoupling plays a central role in the transition from organised roll convection to open-

https://doi.org/10.5194/egusphere-2026-554
Preprint. Discussion started: 11 February 2026

cellular convection. Enhanced precipitation, often driven by secondary ice production and riming, has been shown to promote evaporation and sublimation below the cloud, thereby cooling and moistening the sub-cloud layer. This preconditioning in water vapour at lower levels accelerates the breakup of stratocumulus decks and favours the onset of cellular convection. As a result, the surface supply of moisture and heat to the cloud layer is reduced, weakening roll structures and promoting the development of cellular patterns (Abel et al., 2017; Tornow et al., 2021; Karalis et al., 2022; Wu et al., 2025). A slightly different form of decoupling that does not involve precipitation has been proposed earlier by Bretherton and Wyant (1997), showing that during deepening marine subtropical stratocumulus-topped ABLs a layer of negative buoyancy flux $\overline{w'\vartheta_v'}$ can form below cloud base, as a result of top-down and bottom-up driven mixing becoming too far separated in the vertical. This negative buoyancy flux layer then disrupts the ABL-deep circulation, inducing decoupling.

Both mechanisms of decoupling and the link to graupel formation are investigated next. The buoyancy-based decoupling mechanism is assessed by defining a decoupling point $D_{\overline{w'\vartheta_v'}}$ as the time point at which $\overline{w'\vartheta_v'}$ becomes negative below cloud base for the first time, and remains so until the end of the simulation (indicated as ▼ in Figure 8). The humidity-based decoupling mechanism involving precipitation evaporation is assessed by defining a second decoupling point, this time inferred from Δq_t and $\Delta\vartheta_l$ denoted D_{q_t,ϑ_l}, as discussed above (Section 5.1). Comparing these two definitions gives insight into how exactly decoupling works in MCAOs and how it affects the shifts in ice phase hydrometeors.

Figure 12 compares the locations of the largest peaks in liquid water path ($LWP_{\max}$), graupel water path ($GIWP_{\max}$), and surface precipitation rate ($P_{\text{tot, max}}$) with the two decoupling points D_{q_t,ϑ_l} and $D_{\overline{w'\vartheta_v'}}$, for all simulations except Sub200 (in which no graupel appears). A key result that stands out is that buoyancy-based decoupling (vertical axis) structurally happens first, in all simulations (also indicated in Figure 8). This is followed by the peak in LWP, then integrated graupel, then surface precipitation, and finally the precipitation-based decoupling point. This sequence of events typically covers 1 degree of latitude in this MCAO case, and shifts southward with increasing prescribed mesoscale subsidence. The order of appearance of the various maxima is consistent with the idea that i) internal buoyancy-decoupling initiates events and causes stronger surface-driven convection, ii) driving stronger precipitation formation (mainly in graupel form) that efficiently depletes cloud liquid water mass (as discussed by Abel et al., 2017), iii) forming intense graupel for a while, iv) associated with enhanced surface precipitation which then v) further stabilises the lower boundary layer through evaporation below cloud base, suppressing vertical mixing and further enhancing decoupling (Wu et al., 2025). The last step is also suggested by the slight lowering of liquid cloud base height visible in Figure 8. This sequence of events ultimately yields a fully decoupled structure with respect to Δq_t and $\Delta\vartheta_l$ at D_{q_t,ϑ_l}.

6 Conclusions

This study investigates the sensitivity of Arctic mixed-phase cloud evolution in developing marine cold air outbreaks with respect to mesoscale subsidence, using a Lagrangian Large-Eddy Simulation framework constrained by HALO–$(\mathcal{AC})^3$ observations. The control simulation was evaluated against an extensive and independent set of airborne in-situ and remote-sensing and meteorological balloon measurements. In the control run, the model reproduced the vertical thermodynamic structure of the

https://doi.org/10.5194/egusphere-2026-554
Preprint. Discussion started: 11 February 2026

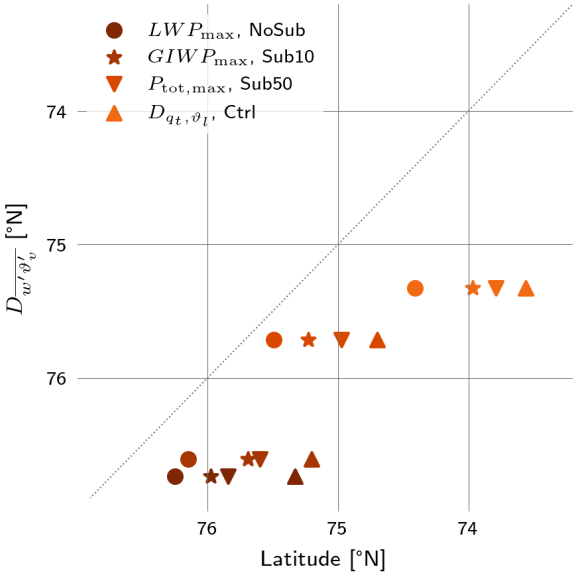

Figure 12. Location of the largest peak in liquid water path $LWP_{\max}$, graupel water path $GIWP_{\max}$ and precipitation $P_{\text{tot, max}}$ and the location of decoupling with respect to the q_t and ϑ_l profiles D_{q_t,ϑ_l} (following Jones et al. (2011)) in relation to the location of decoupling with respect to the buoyancy flux $D_{\overline{w'\vartheta'_v}}$ (following Bretherton and Wyant (1997)). The colours represent the different simulation experiments as in Figure 11. The grey dashed line indicates the identity.

observed marine cold air outbreak reasonably well, capturing the evolution of air temperature, humidity, and ABL height along the Lagrangian trajectory. Compared to dropsonde, radiometer, and lidar data, the simulation accurately represented the integrated water vapour and liquid water path, with a slight cold and dry bias at lower levels. The general agreement demonstrates that the applied forcing and initialisation derived from the HALO–$(\mathcal{AC})^3$ measurements provide a robust foundation for reproducing the dynamics and properties of the Arctic atmospheric boundary layer, underscoring the importance of constraining simulations with detailed observations.

Sensitivity experiments with the tested model revealed that subsidence exerts a strong control on the depth of the atmospheric boundary layer, the height of the cloud top, and the partitioning between the liquid and ice phases in clouds. Weak or absent subsidence enables deeper growth of the atmospheric boundary layer, allowing it to approach the theoretical parabolic deepening rate implied by standard bulk mixed-layer modelling. Reduced subsidence also enhances convective overturning, promoting stronger mixed-phase cloud formation and an earlier onset of (also stronger) graupel formation. In contrast, strong subsidence (Sub200) suppresses vertical development and convective activity, leading to thinner and shorter-lived clouds. The earlier and more pronounced graupel peak in the weak-subsidence cases, and an apparent time-correlation with the formation of a decoupled vertical structure in the cloud field (Figure 9) indicates that graupel formation is tightly linked to the onset of significant surface-driven convection featuring moist updrafts.

https://doi.org/10.5194/egusphere-2026-554
Preprint. Discussion started: 11 February 2026

A deeper analysis of the decoupling process provides an additional perspective on these dynamical–microphysical interactions. Two expressions of decoupling are investigated: (i) one based on the buoyancy flux profile, and (ii) the other reflecting the internal vertical thermodynamic structure of the atmospheric boundary layer. A systematic dependence of the onset of decoupling on the prescribed subsidence is identified, indicating an earlier convective transition in cases with reduced subsidence. Buoyancy-based decoupling always happens first, closely followed by (i) a distinct maximum in the cloud liquid water path, (ii) a peak in the graupel path, (iii) a peak in surface precipitation, and (iv) complete thermodynamic decoupling. This robust order of events and its southward shift with increasing subsidence further highlight the role of subsidence in the transformation of air masses during marine cold air outbreaks. Its impact on the atmospheric boundary layer depth plays a crucial role, promoting buoyancy decoupling below cloud base, which subsequently induces precipitation-driven stabilisation at low levels by accelerating the depletion of the cloud liquid water through graupel formation. This sequence of events eventually drives a transition toward a fully decoupled structure and to open cellular convection later on. These results underscore that subsidence not only constrains the atmospheric boundary layer and cloud depth but also controls the mixed-phase partitioning and the timing of falling hydrometeor formation during marine cold air outbreaks.

These results highlight the role of subsidence in shaping the structure and lifetime of Arctic mixed-phase clouds, although they are based on a single case study. Their applicability across different Arctic conditions, particularly during stronger marine cold air outbreaks, has not yet been assessed. Accordingly, future work should extend this analysis to additional cases and explore how the sensitivity to subsidence compares to variations in other factors, including aerosol and ice-nucleating particle (INP) concentrations. Such investigations will help to disentangle the relative importance of dynamical versus microphysical controls across scales on mixed-phase cloud evolution in the convective atmospheric boundary layer at high latitudes.

Code and data availability. The pre-processed dropsondes data are available at George et al. (2024), and the regression processing followed Paulus et al. (2024); Paulus and Karalis (2023). The integrated water vapour and liquid water path retrieved from HAMP and MiRAC observations will be published to the Pangaea repository soon and will be openly available until acceptance of the manuscript, at the latest; until then, the data can be obtained from the corresponding author upon request. Radar reflectivities from MiRAC used for the retrieval of ice water path are available at Mech et al. (2024) and can be accessed via the ac3airborne tool (Mech et al., 2022). VELOX two-dimensional cloud-top and surface brightness temperatures with 1 Hz temporal resolution, derived at flight altitude, are available from Schäfer et al. (2023). The CMET data is also being prepared for publication and will be publicly available on the Pangaea repository until acceptance of this manuscript. The model code, input and configuration files, generated forcing files, and selected model output are provided in Paulus (2026). The forcing files are compatible with typical single-column model (SCM) forcings, as DALES is run with horizontally homogeneous initial and boundary conditions. The DALES version used in this study is 4.3 with an extension for mixed-phase microphysics; the specific version applied here is included in Paulus (2026), while the official DALES repository is available at Arabas et al. (2021). ERA5 datasets were retrieved from the Copernicus Climate Change Service (C3S) Climate Data Store (CDS) at https://cds.climate.copernicus.eu/.

https://doi.org/10.5194/egusphere-2026-554
Preprint. Discussion started: 11 February 2026

Appendix A: Cold air outbreak and stability indices

Following Papritz and Spengler (2017) and Dahlke et al. (2022), the MCAO Index M is defined as the difference between the sea surface potential temperature ϑ_{SKT} and the potential temperature at $850\,\mathrm{hPa}$ $\vartheta_{850\,\mathrm{hPa}}$:

$$M = \vartheta_{\mathrm{SKT}} - \vartheta_{850\,\mathrm{hPa}} \tag{A1}$$

Positive values indicate enhanced instability, favouring convection and cloud formation, while negative values point to a more stable boundary layer. Papritz and Spengler (2017) identify MCAO conditions if $M > 0\,\mathrm{K}$ and classify MCAOs as weak ($0\,\mathrm{K} < M \leq 4\,\mathrm{K}$), moderate ($4\,\mathrm{K} < M \leq 8\,\mathrm{K}$), strong ($8\,\mathrm{K} < M \leq 12\,\mathrm{K}$) and very strong ($M > 12\,\mathrm{K}$). In Figure A1 we present M as a function of latitude following the Lagrangian trajectory of the modelled air mass for the Ctrl simulation calculated from the model output, together with an estimation of M from the surface and dropsonde observations, using temperature and pressure profiles averaged over all sondes in one circle at the height level closest to $850\,\mathrm{hPa}$ for comparison.

The Stability Index is expressed as the ratio $\frac{z_i}{L}$, where z_i is the boundary-layer height, diagnosed from the model as the minimum local gradient of virtual potential temperature, and calculated from the averaged dropsonde profiles as the level that reaches a critical value of the bulk Richardson number $Ri_{b,\mathrm{crit}} > 0.25$ (ECMWF, 2016; Troen and Mahrt, 1986). The Obukhov length L characterises the role of buoyancy in turbulent flows:

$$L = -\frac{u_*^3 \overline{\vartheta_v}}{\kappa g (\overline{w'\vartheta_v'})_s} \tag{A2}$$

with frictional velocity u_*, mean virtual potential temperature $\overline{\vartheta_v}$, surface virtual potential temperature flux $(\overline{w'\vartheta_v'})_s$ and Kármán constant κ (Stull, 1988). L is included in the model output and can be estimated from observations using a similar method by applying Monin–Obukhov similarity theory and iteratively solving the stability functions for L using Ri_b as an initial guess (Heus et al., 2010).

A1 Trajectory calculation

Appendix B: Statistics of observed mesoscale subsidence

Appendix C: Mean absolute percentage error and agreement

To calculate the agreement of the simulation with the observational data, this study uses the mean absolute percentage error (MAPE)

$$\mathrm{MAPE} = \frac{100\,\%}{n} \sum_{i=1}^{n} \left| \frac{S_i - O_i}{O_i} \right| \tag{C1}$$

with the simulation output S_i and the observational data O_i. It follows:

$$\mathrm{Agreement} = 100\,\% - \mathrm{MAPE}\,. \tag{C2}$$

https://doi.org/10.5194/egusphere-2026-554
Preprint. Discussion started: 11 February 2026

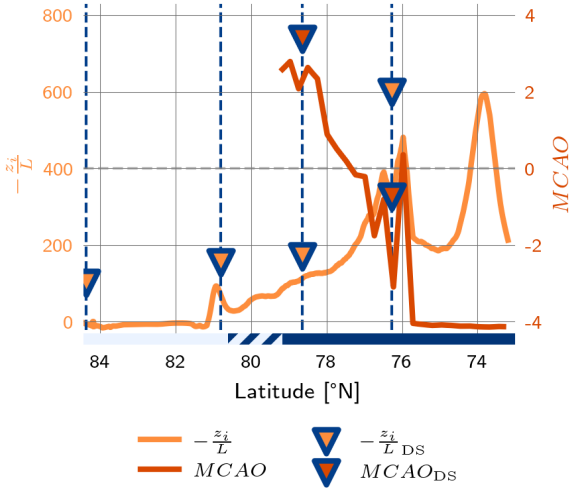

Figure A1. MCAO Index from Ctrl model output (red line) and from surface observations using VELOX and dropsonde profiles (red triangles). Stability index $-\frac{z_i}{L}$ from Ctrl model output (yellow line) and from observations (yellow triangles) along the simulation trajectory.

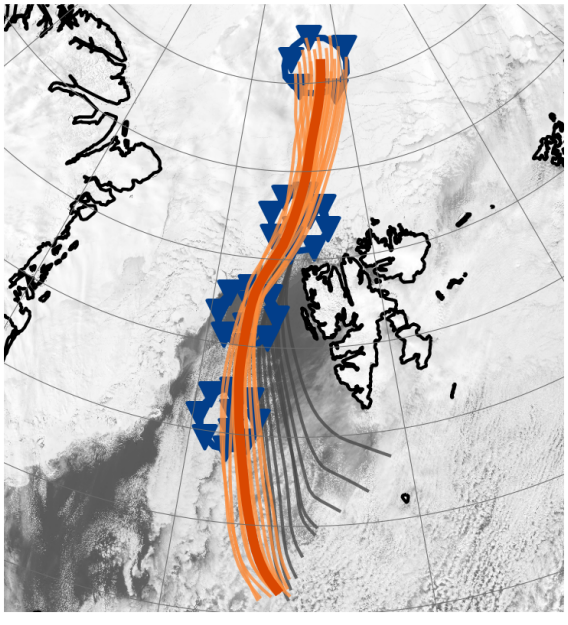

Figure A2. Lagrangian trajectories initiated inside IC at 870 hPa that were recaptured in C01, C02 and C03 (orange). Trajectories that were not resampled in the subsequent circle were discarded (grey) from the calculation of the mean trajectory used for the simulation (red). Dropsonde locations are marked with ▼. Satellite image at the time of RF11 March 29, 2022 from Terra MODIS (NASA (2022), Worldview Snapshots) in the background.

https://doi.org/10.5194/egusphere-2026-554
Preprint. Discussion started: 11 February 2026

Table B1. Summary of subsidence statistics derived from dropsonde observations for each circle. Mean values are computed over the full 8 km profile, while ranges and uncertainty estimates refer to the lowest 3 km.

Circle	Mean (8 km)		Range (3 km)		Mean error (3 km)		Error range (3 km)	
	$[\mathrm{Pa\,s^{-1}}]$	$[\mathrm{cm\,s^{-1}}]$	$[\mathrm{Pa\,s^{-1}}]$	$[\mathrm{cm\,s^{-1}}]$	$[\mathrm{Pa\,s^{-1}}]$	$[\mathrm{cm\,s^{-1}}]$	$[\mathrm{Pa\,s^{-1}}]$	$[\mathrm{cm\,s^{-1}}]$
IC	0.08	−0.74	0 to 0.11	−1.17 to 0	0.002	0.018	0 to 0.002	0 to 0.025
C01	−0.01	0.12	−0.08 to 0.01	−0.07 to 0.82	0.001	0.008	0 to 0.001	0 to 0.012
C02	0.07	−0.60	0 to 0.13	−1.16 to 0	0.001	0.006	0 to 0.001	0.001 to 0.009
C03	0.03	−0.26	0 to 0.08	−0.71 to 0	0.001	0.005	0.000 to 0.001	0.000 to 0.008

Author contributions. The authors made distinct contributions to the project. FP ran and evaluated the simulations and prepared the manuscript. JM determined the surface temperature from VELOX; BK calculated the Lagrangian trajectories; LvG and AW calculated the integrated water vapour from HAMP and the ice water path from MiRAC, respectively; and HS contributed the CMET observations, and MW and RN revised various intermediate versions of the manuscript.

Competing interests. The contact author has declared that none of the authors has any competing interests.

Acknowledgements. We gratefully acknowledge the funding by the Deutsche Forschungsgemeinschaft (DFG; German Research Foundation) - Project 268020496-TRR 172, within the Transregional Collaborative Research Center "Arctic Amplification: Climate Relevant Atmospheric and Surface Processes, and Feedback Mechanisms $(\mathcal{AC})^3$." We are further grateful for the funding of Project Grant 316646266 by the DFG (German Research Foundation) within the framework of Priority Programme SPP 1294 to promote research with HALO. We also gratefully acknowledge the funding by the DFG (German Research Foundation) - Project 442649391 - Observing Local and Remote Controls on Arctic Air Mass Evolution (ORCA2). We gratefully acknowledge the Gauss Centre for Supercomputing e.V. (www.gauss-centre.eu) for providing computing time on the GCS Supercomputer JUWELS at the Jülich Supercomputing Centre (JSC) under projects RCONGM and HR-AFC. We appreciate the financial contributions of the Alfred Wegener Institute (AWI, Bremerhaven), the German Aerospace Centre (DLR, Oberpfaffenhofen), and the Max Planck Institute for Meteorology (MPI-M, Hamburg). HS acknowledges funding from the European Research Council within the H-2020 programe (Isotopic Links to Atmospheric Water's Sources (ISLAS), grant nr. 773245). We acknowledge the use of imagery from the Worldview Snapshots application (https://wvs.earthdata.nasa.gov), part of the Earth Observing System Data and Information System (EOSDIS). ChatGPT-4o has been used to help create the first versions of this manuscript. Thank you to Niklas Schnierstein and Jan Chylik for developing the DALES-CGN model with representation of Arctic mixed-phase clouds. At last, we want to acknowledge and thank everyone involved in the HALO–$(\mathcal{AC})^3$and ISLAS2022 campaigns, especially Mario Mech, who kindly provided the liquid water path data from MiRAC for this study.

https://doi.org/10.5194/egusphere-2026-554
Preprint. Discussion started: 11 February 2026

References

Abel, S. J., Boutle, I. A., Waite, K., Fox, S., Brown, P. R. A., Cotton, R., Lloyd, G., Choularton, T. W., and Bower, K. N.: The Role of Precipitation in Controlling the Transition from Stratocumulus to Cumulus Clouds in a Northern Hemisphere Cold-Air Outbreak, Journal of the Atmospheric Sciences, 74, 2293–2314, https://doi.org/10.1175/JAS-D-16-0362.1, publisher: American Meteorological Society Section: Journal of the Atmospheric Sciences, 2017.

Ansmann, A., Ohneiser, K., Engelmann, R., Radenz, M., Griesche, H., Hofer, J., Althausen, D., Creamean, J. M., Boyer, M. C., Knopf, D. A., Dahlke, S., Maturilli, M., Gebauer, H., Bühl, J., Jimenez, C., Seifert, P., and Wandinger, U.: Annual cycle of aerosol properties over the central Arctic during MOSAiC 2019–2020 – light-extinction, CCN, and INP levels from the boundary layer to the tropopause, Atmospheric Chemistry and Physics, 23, 12 821–12 849, https://doi.org/10.5194/acp-23-12821-2023, 2023.

Arabas, S., Axelsen, S., Attema, J., Beets, C., Boeing, S. J., de Bruine, M., Chylik, J., Cuijpers, H., van der Dussen, J., van Heerwaarden, C., Heus, T., Jansson, F., Jonker, H., Moene, A., Ouwersloot, H., van den Oord, G., de Roode, S., Neggers, R., Pedruzo, X., Siebesma, P., Sikma, M., van Stratum, B., Vila, J., and van Zanten, M.: dalesteam/dales: DALES 4.3, https://doi.org/10.5281/zenodo.4604726, 2021.

Atkinson, B. W. and Wu Zhang, J.: Mesoscale shallow convection in the atmosphere, Reviews of Geophysics, 34, 403–431, https://doi.org/10.1029/96RG02623, 1996.

Baran, A. J.: The dependence of cirrus infrared radiative properties on ice crystal geometry and shape of the size-distribution function, Quarterly Journal of the Royal Meteorological Society, 131, 1129–1142, https://doi.org/10.1256/qj.04.91, _eprint: https://rmets.onlinelibrary.wiley.com/doi/pdf/10.1256/qj.04.91, 2005.

Bony, S. and Stevens, B.: Measuring area-averaged vertical motions with dropsondes, Journal of the Atmospheric Sciences, 76, 767–783, https://doi.org/10.1175/jas-d-18-0141.1, 2019.

Bretherton, C. S. and Wyant, M. C.: Moisture Transport, Lower-Tropospheric Stability, and Decoupling of Cloud-Topped Boundary Layers, Journal of the Atmospheric Sciences, 54, 148–167, https://doi.org/10.1175/1520-0469(1997)054<0148:MTLTSA>2.0.CO;2, 1997.

Brümmer, B.: Boundary Layer Mass, Water, and Heat Budgets in Wintertime Cold-Air Outbreaks from the Arctic Sea Ice, Monthly Weather Review, 125, 1824–1837, https://doi.org/10.1175/1520-0493(1997)125<1824:BLMWAH>2.0.CO;2, 1997.

Chylik, J., Chechin, D., Dupuy, R., Kulla, B. S., Lüpkes, C., Mertes, S., Mech, M., and Neggers, R.: Aerosol impacts on the entrainment efficiency of Arctic mixed-phase convection in a simulated air mass over open water, Atmospheric Chemistry and Physics, 23, 4903–4929, https://doi.org/10.5194/acp-23-4903-2023, 2023.

Corbetta, G., Orlandi, E., Heus, T., Neggers, R., and Crewell, S.: Overlap statistics of shallow boundary layer clouds: Comparing ground-based observations with large-eddy simulations, Geophysical Research Letters, 42, 8185–8191, https://doi.org/10.1002/2015GL065140, _eprint: https://agupubs.onlinelibrary.wiley.com/doi/pdf/10.1002/2015GL065140, 2015.

Dahlke, S., Solbès, A., and Maturilli, M.: Cold air outbreaks in Fram Strait: climatology, trends, and observations during an extreme season in 2020, Journal Of Geophysical Research: Atmospheres, https://doi.org/10.1029/2021jd035741, 2022.

de Roode, S. R., Frederikse, T., Siebesma, A. P., Ackerman, A. S., Chylik, J., Field, P. R., Fricke, J., Gryschka, M., Hill, A., Honnert, R., Krueger, S. K., Lac, C., Lesage, A. T., and Tomassini, L.: Turbulent Transport in the Gray Zone: A Large Eddy Model Intercomparison Study of the CONSTRAIN Cold Air Outbreak Case, Journal of Advances in Modeling Earth Systems, 11, 597–623, https://doi.org/10.1029/2018MS001443, _eprint: https://agupubs.onlinelibrary.wiley.com/doi/pdf/10.1029/2018MS001443, 2019.

https://doi.org/10.5194/egusphere-2026-554
Preprint. Discussion started: 11 February 2026

Deardorff, J. W.: Stratocumulus-capped mixed layers derived from a three-dimensional model, Boundary-Layer Meteorology, 18, 495–527, https://doi.org/10.1007/BF00119502, 1980.

ECMWF: IFS documentation CY43R1 - Part IV: Physical processes—IFS documentation CY43R1, 2016.

Egerer, U., Ehrlich, A., Gottschalk, M., Griesche, H., Neggers, R. A. J., Siebert, H., and Wendisch, M.: Case study of a humidity layer above Arctic stratocumulus and potential turbulent coupling with the cloud top, Atmospheric Chemistry and Physics, 21, 6347–6364, https://doi.org/10.5194/acp-21-6347-2021, publisher: Copernicus GmbH, 2021.

Ehrlich, A., Crewell, S., Herber, A., Klingebiel, M., Lüpkes, C., Mech, M., Becker, S., Borrmann, S., Bozem, H., Buschmann, M., Clemen, H.-C., De La Torre Castro, E., Dorff, H., Dupuy, R., Eppers, O., Ewald, F., George, G., Giez, A., Grawe, S., Gourbeyre, C., Hartmann, J., Jäkel, E., Joppe, P., Jourdan, O., Jurányi, Z., Kirbus, B., Lucke, J., Luebke, A. E., Maahn, M., Maherndl, N., Mallaun, C., Mayer, J., Mertes, S., Mioche, G., Moser, M., Müller, H., Pörtge, V., Risse, N., Roberts, G., Rosenburg, S., Röttenbacher, J., Schäfer, M., Schaefer, J., Schäfler, A., Schirmacher, I., Schneider, J., Schnitt, S., Stratmann, F., Tatzelt, C., Voigt, C., Walbröl, A., Weber, A., Wetzel, B., Wirth, M., and Wendisch, M.: A comprehensive in situ and remote sensing data set collected during the HALO–$(AC)^3$ aircraft campaign, Earth System Science Data, 17, 1295–1328, https://doi.org/10.5194/essd-17-1295-2025, publisher: Copernicus GmbH, 2025.

Etling, D. and Brown, R. A.: Roll vortices in the planetary boundary layer: A review, Boundary-Layer Meteorology, 65, 215–248, https://doi.org/10.1007/BF00705527, 1993.

Fletcher, J. K., Mason, S., and Jakob, C.: The Climatology, Meteorology, and Boundary Layer Structure of Marine Cold Air Outbreaks in Both Hemispheres, Journal of Climate, 29, 1999–2014, https://doi.org/10.1175/jcli-d-15-0268.1, mAG ID: 2288559338 S2ID: 6a3363926952b8c3d5eaf7bb242dcf31f8355341, 2016.

Fu, Q. and Liou, K. N.: Parameterization of the Radiative Properties of Cirrus Clouds, Journal of Atmospheric Sciences, https://journals.ametsoc.org/view/journals/atsc/50/13/1520-0469_1993_050_2008_potrpo_2_0_co_2.xml, section: Journal of the Atmospheric Sciences, 1993.

Geerts, B., Giangrande, S. E., McFarquhar, G. M., Xue, L., Abel, S. J., Comstock, J. M., Crewell, S., DeMott, P. J., Ebell, K., Field, P., Hill, T. C. J., Hunzinger, A., Jensen, M. P., Johnson, K. L., Juliano, T. W., Kollias, P., Kosovic, B., Lackner, C., Luke, E., Lüpkes, C., Matthews, A. A., Neggers, R., Ovchinnikov, M., Powers, H., Shupe, M. D., Spengler, T., Swanson, B. E., Tjernström, M., Theisen, A. K., Wales, N. A., Wang, Y., Wendisch, M., and Wu, P.: The COMBLE Campaign: A Study of Marine Boundary Layer Clouds in Arctic Cold-Air Outbreaks, Bulletin of the American Meteorological Society, https://doi.org/10.1175/BAMS-D-21-0044.1, section: Bulletin of the American Meteorological Society, 2022.

George, G., Stevens, B., Bony, S., Pincus, R., Fairall, C., Schulz, H., Kölling, T., Kalen, Q. T., Klingebiel, M., Konow, H., Lundry, A., Prange, M., and Radtke, J.: JOANNE: Joint dropsonde Observations of the Atmosphere in tropical North atlaNtic meso-scale Environments, Earth System Science Data, 13, 5253–5272, https://doi.org/10.5194/essd-13-5253-2021, publisher: Copernicus GmbH, 2021.

George, G., Luebke, A. E., Klingebiel, M., Mech, M., and Ehrlich, A.: Dropsonde measurements from HALO and POLAR 5 during HALO-$(AC)^3$ in 2022, https://doi.org/10.1594/PANGAEA.968891, 2024.

Grachev, A. A., Andreas, E. L., Fairall, C. W., Guest, P. S., and Persson, P. O. G.: SHEBA flux–profile relationships in the stable atmospheric boundary layer, Boundary-Layer Meteorology, 124, 315–333, https://doi.org/10.1007/s10546-007-9177-6, 2007.

Hartmann, J., Kottmeier, C., and Raasch, S.: Roll Vortices and Boundary-Layer Development during a Cold Air Outbreak, Boundary-Layer Meteorology, 84, 45–65, https://doi.org/10.1023/A:1000392931768, 1997.

https://doi.org/10.5194/egusphere-2026-554
Preprint. Discussion started: 11 February 2026

Hartmann, M., Blunier, T., Brügger, S., Schmale, J., Schwikowski, M., Vogel, A., Wex, H., and Stratmann, F.: Variation of Ice Nucleating Particles in the European Arctic Over the Last Centuries, Geophysical Research Letters, 46, 4007–4016, https://doi.org/10.1029/2019GL082311, 2019.

Hersbach, H., Bell, B., Berrisford, P., Hirahara, S., Horányi, A., Muñoz-Sabater, J., Nicolas, J., Peubey, C., Radu, R., Schepers, D., Simmons, A., Soci, C., Abdalla, S., Abellan, X., Balsamo, G., Bechtold, P., Biavati, G., Bidlot, J., Bonavita, M., De Chiara, G., Dahlgren, P., Dee, D., Diamantakis, M., Dragani, R., Flemming, J., Forbes, R., Fuentes, M., Geer, A., Haimberger, L., Healy, S., Hogan, R. J., Hólm, E., Janisková, M., Keeley, S., Laloyaux, P., Lopez, P., Lupu, C., Radnoti, G., de Rosnay, P., Rozum, I., Vamborg, F., Villaume, S., and Thépaut, J.-N.: The ERA5 global reanalysis, Quarterly Journal of the Royal Meteorological Society, 146, 1999–2049, https://doi.org/10.1002/qj.3803, _eprint: https://rmets.onlinelibrary.wiley.com/doi/pdf/10.1002/qj.3803, 2020.

Heus, T., van Heerwaarden, C. C., Jonker, H. J. J., Siebesma, A. P., Axelsen, S. L., van den Dries, K., Geoffroy, O., Moene, A. F., Pino, D., de Roode, S. R., and de Arellano, J. V.-G.: Formulation of the Dutch Atmospheric Large-Eddy Simulation (DALES) and overview of its applications, Geoscientific Model Development, 3, 415–444, https://doi.org/10.5194/gmd-3-415-2010, 2010.

Hock, T. F. and Franklin, J. L.: The NCAR GPS Dropwindsonde, Bulletin of the American Meteorological Society, https://journals.ametsoc.org/view/journals/bams/80/3/1520-0477_1999_080_0407_tngd_2_0_co_2.xml, section: Bulletin of the American Meteorological Society, 1999.

Hogan, R. J., Mittermaier, M. P., and Illingworth, A. J.: The Retrieval of Ice Water Content from Radar Reflectivity Factor and Temperature and Its Use in Evaluating a Mesoscale Model, Journal of Applied Meteorology and Climatology, 45, 301–317, https://doi.org/10.1175/JAM2340.1, publisher: American Meteorological Society Section: Journal of Applied Meteorology and Climatology, 2006.

Hundsdorfer, W., Koren, B., vanLoon, M., and Verwer, J. G.: A Positive Finite-Difference Advection Scheme, Journal of Computational Physics, 117, 35–46, https://doi.org/10.1006/jcph.1995.1042, 1995.

Inoue, J., Tobo, Y., Taketani, F., and Sato, K.: Oceanic Supply of Ice-Nucleating Particles and Its Effect on Ice Cloud Formation: A Case Study in the Arctic Ocean During a Cold-Air Outbreak in Early Winter, Geophysical Research Letters, 48, e2021GL094 646, https://doi.org/10.1029/2021GL094646, _eprint: https://agupubs.onlinelibrary.wiley.com/doi/pdf/10.1029/2021GL094646, 2021.

Isachsen, P. E., Drivdal, M., Eastwood, S., Gusdal, Y., Noer, G., and Saetra, O.: Observations of the ocean response to cold air outbreaks and polar lows over the Nordic Seas, Geophysical Research Letters, 40, 3667–3671, https://doi.org/10.1002/grl.50705, 2013.

Jones, C. R., Bretherton, C. S., and Leon, D.: Coupled vs. decoupled boundary layers in VOCALS-REx, Atmospheric Chemistry and Physics, 11, 7143–7153, https://doi.org/10.5194/acp-11-7143-2011, 2011.

Karalis, M., Sotiropoulou, G., Abel, S. J., Bossioli, E., Georgakaki, P., Methymaki, G., Nenes, A., and Tombrou, M.: Effects of secondary ice processes on a stratocumulus to cumulus transition during a cold-air outbreak, Atmospheric Research, 277, 106 302, https://doi.org/10.1016/j.atmosres.2022.106302, 2022.

Kirbus, B., Chylik, J., Ehrlich, A., Becker, S., Schäfer, M., Neggers, R., and Wendisch, M.: Analysis of an Arctic cold air outbreak during autumn and related air mass transformations forced by surface changes and advection in higher altitudes, Elementa: Science of the Anthropocene, 11, 00 079, https://doi.org/10.1525/elementa.2023.00079, 2023.

Kirbus, B., Schirmacher, I., Klingebiel, M., Schäfer, M., Ehrlich, A., Slättberg, N., Lucke, J., Moser, M., Müller, H., and Wendisch, M.: Thermodynamic and cloud evolution in a cold-air outbreak during HALO-(AC)3: quasi-Lagrangian observations compared to the ERA5 and CARRA reanalyses, Atmospheric Chemistry and Physics, https://doi.org/10.5194/acp-24-3883-2024, 2024.

https://doi.org/10.5194/egusphere-2026-554
Preprint. Discussion started: 11 February 2026

Klingebiel, M., Ehrlich, A., Gryschka, M., Risse, N., Maherndl, N., Schirmacher, I., Rosenburg, S., Hörnig, S., Moser, M., Jäkel, E., Schäfer, M., Deneke, H., Mech, M., Voigt, C., and Wendisch, M.: Airborne observations of cloud properties during their evolution from organized streets to isotropic cloud structures along an Arctic cold-air outbreak, Atmospheric Chemistry and Physics, 25, 9787–9801, https://doi.org/10.5194/acp-25-9787-2025, 2025.

Kolstad, E. W.: Higher ocean wind speeds during marine cold air outbreaks, Quarterly Journal of the Royal Meteorological Society, 143, 2084–2092, https://doi.org/10.1002/qj.3068, 2017.

Laar, T. W. v., Schemann, V., and Neggers, R. A. J.: Investigating the Diurnal Evolution of the Cloud Size Distribution of Continental Cumulus Convection Using Multiday LES, Journal of Atmospheric Sciences, https://doi.org/10.1175/JAS-D-18-0084.1, section: Journal of the Atmospheric Sciences, 2019.

Lenschow, D. H. and Agee, E. M.: Preliminary Results from the Air Mass Transformation Experiment (AMTEX), Bulletin of the American Meteorological Society, 57, 1346–1355, https://doi.org/10.1175/1520-0477-57.11.1346, 1976.

Lenschow, D. H., Savic-Jovcic, V., and Stevens, B.: Divergence and Vorticity from Aircraft Air Motion Measurements, Journal of Atmospheric and Oceanic Technology, https://doi.org/10.1175/2007JTECHA940.1, section: Journal of Atmospheric and Oceanic Technology, 2007.

Lloyd, G., Choularton, T. W., Bower, K. N., Gallagher, M. W., Crosier, J., O'Shea, S., Abel, S. J., Fox, S., Cotton, R., and Boutle, I. A.: In situ measurements of cloud microphysical and aerosol properties during the break-up of stratocumulus cloud layers in cold air outbreaks over the North Atlantic, Atmospheric Chemistry and Physics, 18, 17 191–17 206, https://doi.org/10.5194/acp-18-17191-2018, 2018.

Løklingholm, S., Johannessen, A. M., Sodemann, H., Hole, L. R., and Voss, P.: Evaluating the quality and additional value of Controlled Meteorological Balloons to observe air mass transformation during marine cold-air outbreaks, to be submitted to JGR-Atmopsheres, 2026.

Marcheggiani, A. and Spengler, T.: Cold air outbreaks drive near-surface baroclinicity variability over storm track entrance regions in the Northern Hemisphere, Weather and Climate Dynamics, 6, 1479–1489, https://doi.org/10.5194/wcd-6-1479-2025, 2025.

Mateling, M. E., Pettersen, C., Kulie, M. S., and L'Ecuyer, T. S.: Marine Cold-Air Outbreak Snowfall in the North Atlantic: A CloudSat Perspective, Journal of Geophysical Research: Atmospheres, 128, e2022JD038 053, https://doi.org/10.1029/2022JD038053, 2023.

McCoy, I. L., Wood, R., and Fletcher, J. K.: Identifying Meteorological Controls on Open and Closed Mesoscale Cellular Convection Associated with Marine Cold Air Outbreaks, Journal of Geophysical Research: Atmospheres, 122, 11,678–11,702, https://doi.org/10.1002/2017JD027031, 2017.

McFarquhar, G. M. and Heymsfield, A. J.: The Definition and Significance of an Effective Radius for Ice Clouds, Journal of Atmospheric Sciences, https://journals.ametsoc.org/view/journals/atsc/55/11/1520-0469_1998_055_2039_tdasoa_2.0.co_2.xml, section: Journal of the Atmospheric Sciences, 1998.

Mech, M., Orlandi, E., Crewell, S., Ament, F., Hirsch, L., Hagen, M., Peters, G., and Stevens, B.: HAMP – the microwave package on the High Altitude and LOng range research aircraft (HALO), Atmospheric Measurement Techniques, 7, 4539–4553, https://doi.org/10.5194/amt-7-4539-2014, publisher: Copernicus GmbH, 2014.

Mech, M., Kliesch, L.-L., Anhäuser, A., Rose, T., Kollias, P., and Crewell, S.: Microwave Radar/radiometer for Arctic Clouds (MiRAC): first insights from the ACLOUD campaign, Atmospheric Measurement Techniques, 12, 5019–5037, https://doi.org/10.5194/amt-12-5019-2019, publisher: Copernicus GmbH, 2019.

Mech, M., Risse, N., Marrollo, G., and Paul, D.: ac3airborne, https://zenodo.org/records/7305586, 2022.

https://doi.org/10.5194/egusphere-2026-554
Preprint. Discussion started: 11 February 2026

Mech, M., Risse, N., Krobot, P., Paul, D., Schirmacher, I., Schnitt, S., and Crewell, S.: Radar reflectivities at 94 GHz and microwave brightness temperature measurements at 89 GHz during the HALO-AC3 Arctic airborne campaign, https://doi.org/10.1594/PANGAEA.964977, 2024.

Michaelis, J., Schmitt, A. U., Lüpkes, C., Hartmann, J., Birnbaum, G., and Vihma, T.: Observations of marine cold-air outbreaks: a comprehensive data set of airborne and dropsonde measurements from the Springtime Atmospheric Boundary Layer Experiment (STABLE), Earth System Science Data, 14, 1621–1637, https://doi.org/10.5194/essd-14-1621-2022, publisher: Copernicus GmbH, 2022.

Müller, J. J., Schäfer, M., Rosenburg, S., Ehrlich, A., and Wendisch, M.: High-resolution maps of Arctic surface skin temperature and type retrieved from airborne thermal infrared imagery collected during the HALO–$(\mathcal{AC})^3$ campaign, Atmospheric Measurement Techniques, 18, 4695–4708, https://doi.org/10.5194/amt-18-4695-2025, 2025.

Murray-Watson, R. J. and Gryspeerdt, E.: Air mass history linked to the development of Arctic mixed-phase clouds, Atmospheric Chemistry and Physics, 24, 11 115–11 132, https://doi.org/10.5194/acp-24-11115-2024, publisher: Copernicus GmbH, 2024.

Murray-Watson, R. J., Gryspeerdt, E., and Goren, T.: Investigating the development of clouds within marine cold-air outbreaks, Atmospheric Chemistry and Physics, 23, 9365–9383, https://doi.org/10.5194/acp-23-9365-2023, mAG ID: 4386198900 S2ID: 1d8a3f5d85a4055cb6d3c729eb400e243f1856ca, 2023.

NASA: Worldview Snapshots, https://wvs.earthdata.nasa.gov/, 2022.

Neggers, R. A. J., Chylik, J., Egerer, U., Griesche, H., Schemann, V., Seifert, P., Siebert, H., and Macke, A.: Local and Remote Controls on Arctic Mixed-Layer Evolution, Journal of Advances in Modeling Earth Systems, 11, 2214–2237, https://doi.org/10.1029/2019ms001671, mAG ID: 2950203434 S2ID: 9f32a63ae869cd1ce659fd9f12a0708b110c8d57, 2019.

Papritz, L. and Spengler, T.: A Lagrangian Climatology of Wintertime Cold Air Outbreaks in the Irminger and Nordic Seas and Their Role in Shaping Air–Sea Heat Fluxes, Journal of Climate, 30, 2717–2737, https://doi.org/10.1175/jcli-d-16-0605.1, 2017.

Papritz, L., Pfahl, S., Sodemann, H., and Wernli, H.: A Climatology of Cold Air Outbreaks and Their Impact on Air–Sea Heat Fluxes in the High-Latitude South Pacific, Journal of Climate, 28, 342–364, https://doi.org/10.1175/JCLI-D-14-00482.1, 2015.

Paulus, F.: Impacts of mesoscale atmospheric subsidence on cloud glaciation and decoupling in Arctic marine cold air outbreaks [Model configuration and output], https://doi.org/10.5281/zenodo.18232592, 2026.

Paulus, F. and Karalis, M.: Airborne measurements of mesoscale divergence at high latitudes during HALO-(AC)^3 [Code publication], https://doi.org/10.5281/zenodo.10402061, 2023.

Paulus, F. M., Karalis, M., George, G., Svensson, G., Wendisch, M., and Neggers, R. A. J.: Airborne Measurements of Mesoscale Divergence at High Latitudes during HALO–(AC)3, Journal of Atmospheric Sciences, https://doi.org/10.1175/JAS-D-24-0034.1, section: Journal of the Atmospheric Sciences, 2024.

Pincus, R. and Stevens, B.: Monte Carlo Spectral Integration: a Consistent Approximation for Radiative Transfer in Large Eddy Simulations, Journal of Advances in Modeling Earth Systems, 1, https://doi.org/10.3894/JAMES.2009.1.1, _eprint: https://agupubs.onlinelibrary.wiley.com/doi/pdf/10.3894/JAMES.2009.1.1, 2009.

Pithan, F., Svensson, G., Caballero, R., Chechin, D., Cronin, T. W., Ekman, A. M. L., Neggers, R., Shupe, M. D., Solomon, A., Tjernström, M., and Wendisch, M.: Role of air-mass transformations in exchange between the Arctic and mid-latitudes, Nature Geoscience, 11, 805–812, https://doi.org/10.1038/s41561-018-0234-1, publisher: Nature Publishing Group, 2018.

Poujol, B. and Bony, S.: Measuring Clear-Air Vertical Motions From Space, AGU Advances, 5, e2024AV001 267, https://doi.org/10.1029/2024AV001267, 2024.

https://doi.org/10.5194/egusphere-2026-554
Preprint. Discussion started: 11 February 2026

Rasmussen, E. A., Pedersen, T. S., Pedersen, L. T., and Turner, J.: Polar lows and arctic instability lows in the Bear Island region, Tellus A, 44, 133–154, https://doi.org/10.1034/j.1600-0870.1992.t01-1-00004.x, 1992.

Reilly, S., Gesso, S. D., and Neggers, R.: Configuring LES Based on Dropsonde Data in Sparsely Sampled Areas in the Subtropical Atlantic, Journal of Applied Meteorology and Climatology, https://doi.org/10.1175/JAMC-D-19-0013.1, section: Journal of Applied Meteorology and Climatology, 2020.

Renfrew, I. A. and Moore, G. W. K.: An Extreme Cold-Air Outbreak over the Labrador Sea: Roll Vortices and Air–Sea Interaction, Monthly Weather Review, 127, 2379–2394, https://doi.org/10.1175/1520-0493(1999)127<2379:AECAOO>2.0.CO;2, 1999.

Roode, S. R. d., Sandu, I., Dussen, J. J. v. d., Ackerman, A. S., Blossey, P., Jarecka, D., Lock, A., Siebesma, A. P., and Stevens, B.: Large-Eddy Simulations of EUCLIPSE–GASS Lagrangian Stratocumulus-to-Cumulus Transitions: Mean State, Turbulence, and Decoupling, Journal of Atmospheric Sciences, https://doi.org/10.1175/JAS-D-15-0215.1, section: Journal of the Atmospheric Sciences, 2016.

Schäfer, M., Rosenburg, S., Ehrlich, A., Röttenbacher, J., and Wendisch, M.: Two-dimensional cloud-top and surface brightness temperature with 1 Hz temporal resolution derived at flight altitude from VELOX during the HALO-$(AC)^3$ field campaign, https://doi.org/10.1594/PANGAEA.963401, 2023.

Schirmacher, I., Schnitt, S., Klingebiel, M., Maherndl, N., Kirbus, B., Ehrlich, A., Mech, M., and Crewell, S.: Clouds and precipitation in the initial phase of marine cold-air outbreaks as observed by airborne remote sensing, Atmospheric Chemistry and Physics, https://doi.org/10.5194/acp-24-12823-2024, s2ID: 18c789386a2e929d9ce43fba56864e0a84d0254c, 2024.

Schnierstein, N., Chylik, J., Shupe, M. D., and Neggers, R. A. J.: Standardized Daily High-Resolution Large-Eddy Simulations of the Arctic Boundary Layer and Clouds During the Complete MOSAiC Drift, Journal of Advances in Modeling Earth Systems, https://doi.org/10.1029/2024ms004296, 2024.

Schäfer, M., Wolf, K., Ehrlich, A., Hallbauer, C., Jäkel, E., Jansen, F., Luebke, A. E., Müller, J., Thoböll, J., Röschenthaler, T., Stevens, B., and Wendisch, M.: VELOX – a new thermal infrared imager for airborne remote sensing of cloud and surface properties, Atmospheric Measurement Techniques, 15, 1491–1509, https://doi.org/10.5194/amt-15-1491-2022, publisher: Copernicus GmbH, 2022.

Seidel, D. J., Zhang, Y., Beljaars, A., Golaz, J.-C., Jacobson, A. R., and Medeiros, B.: Climatology of the planetary boundary layer over the continental United States and Europe, Journal of Geophysical Research: Atmospheres, 117, https://doi.org/10.1029/2012JD018143, 2012.

Seifert, A. and Beheng, K. D.: A two-moment cloud microphysics parameterization for mixed-phase clouds. Part 1: Model description, Meteorology and Atmospheric Physics, 92, 45–66, https://doi.org/10.1007/s00703-005-0112-4, 2006.

Shapiro, M. A., Fedor, L. S., and Hampel, T.: Research aircraft measurements of a polar low over the Norwegian Sea, Tellus, 39, https://doi.org/10.3402/tellusa.v39i4.11761, 1987.

Shestakova, A. A., Chechin, D. G., Lüpkes, C., Hartmann, J., and Maturilli, M.: The foehn effect during easterly flow over Svalbard, Atmospheric Chemistry and Physics, 22, 1529–1548, https://doi.org/10.5194/acp-22-1529-2022, 2022.

Slättberg, N., Dahlke, S., and Maturilli, M.: Fram Strait Marine Cold Air Outbreaks in CARRA and ERA5: Effects on Surface Turbulent Heat Fluxes and the Vertical Structure of the Troposphere, Journal of Geophysical Research: Atmospheres, 130, e2024JD042 908, https://doi.org/10.1029/2024JD042908, _eprint: https://agupubs.onlinelibrary.wiley.com/doi/pdf/10.1029/2024JD042908, 2025.

Solomon, A., de Boer, G., Creamean, J. M., McComiskey, A., Shupe, M. D., Maahn, M., and Cox, C.: The relative impact of cloud condensation nuclei and ice nucleating particle concentrations on phase partitioning in Arctic mixed-phase stratocumulus clouds, Atmospheric Chemistry and Physics, 18, 17 047–17 059, https://doi.org/10.5194/acp-18-17047-2018, 2018.

https://doi.org/10.5194/egusphere-2026-554
Preprint. Discussion started: 11 February 2026

Spreen, G., Kaleschke, L., and Heygster, G.: Sea ice remote sensing using AMSR-E 89-GHz channels, Journal of Geophysical Research: Oceans, 113, https://doi.org/https://doi.org/10.1029/2005JC003384, 2008.

Sprenger, M. and Wernli, H.: The LAGRANTO Lagrangian analysis tool – version 2.0, Geoscientific Model Development, 8, 2569–2586, https://doi.org/10.5194/gmd-8-2569-2015, publisher: Copernicus GmbH, 2015.

Stachlewska, I. S., Neuber, R., Lampert, A., Ritter, C., and Wehrle, G.: AMALi – the Airborne Mobile Aerosol Lidar for Arctic research, Atmospheric Chemistry and Physics, 2009.

Stevens, B.: On the Growth of Layers of Nonprecipitating Cumulus Convection, Journal of the Atmospheric Sciences, 64, 2916–2931, https://doi.org/10.1175/JAS3983.1, publisher: American Meteorological Society Section: Journal of the Atmospheric Sciences, 2007.

Stevens, B., Ackerman, A. S., Albrecht, B. A., Brown, A. R., Chlond, A., Cuxart, J., Duynkerke, P. G., Lewellen, D. C., Macvean, M. K., Neggers, R. A. J., Sánchez, E., Siebesma, A. P., and Stevens, D. E.: Simulations of Trade Wind Cumuli under a Strong Inversion, Journal of the Atmospheric Sciences, 58, 1870–1891, https://doi.org/10.1175/1520-0469(2001)058<1870:SOTWCU>2.0.CO;2, publisher: American Meteorological Society Section: Journal of the Atmospheric Sciences, 2001.

Stevens, B., Ament, F., Bony, S., Crewell, S., Ewald, F., Gross, S., Hansen, A., Hirsch, L., Jacob, M., Kölling, T., Konow, H., Mayer, B., Wendisch, M., Wirth, M., Wolf, K., Bakan, S., Bauer-Pfundstein, M., Brueck, M., Delanoë, J., Ehrlich, A., Farrell, D., Forde, M., Gödde, F., Grob, H., Hagen, M., Jäkel, E., Jansen, F., Klepp, C., Klingebiel, M., Mech, M., Peters, G., Rapp, M., Wing, A. A., and Zinner, T.: A High-Altitude Long-Range Aircraft Configured as a Cloud Observatory: The NARVAL Expeditions, Bulletin of the American Meteorological Society, https://doi.org/10.1175/BAMS-D-18-0198.1, section: Bulletin of the American Meteorological Society, 2019.

Stevens, B., Bony, S., Farrell, D., Ament, F., Blyth, A., Fairall, C., Karstensen, J., Quinn, P. K., Speich, S., Acquistapace, C., Aemisegger, F., Albright, A. L., Bellenger, H., Bodenschatz, E., Caesar, K.-A., Chewitt-Lucas, R., de Boer, G., Delanoë, J., Denby, L., Ewald, F., Fildier, B., Forde, M., George, G., Gross, S., Hagen, M., Hausold, A., Heywood, K. J., Hirsch, L., Jacob, M., Jansen, F., Kinne, S., Klocke, D., Kölling, T., Konow, H., Lothon, M., Mohr, W., Naumann, A. K., Nuijens, L., Olivier, L., Pincus, R., Pöhlker, M., Reverdin, G., Roberts, G., Schnitt, S., Schulz, H., Siebesma, A. P., Stephan, C. C., Sullivan, P., Touzé-Peiffer, L., Vial, J., Vogel, R., Zuidema, P., Alexander, N., Alves, L., Arixi, S., Asmath, H., Bagheri, G., Baier, K., Bailey, A., Baranowski, D., Baron, A., Barrau, S., Barrett, P. A., Batier, F., Behrendt, A., Bendinger, A., Beucher, F., Bigorre, S., Blades, E., Blossey, P., Bock, O., Böing, S., Bosser, P., Bourras, D., Bouruet-Aubertot, P., Bower, K., Branellec, P., Branger, H., Brennek, M., Brewer, A., Brilouet, P.-E., Brügmann, B., Buehler, S. A., Burke, E., Burton, R., Calmer, R., Canonici, J.-C., Carton, X., Cato Jr., G., Charles, J. A., Chazette, P., Chen, Y., Chilinski, M. T., Choularton, T., Chuang, P., Clarke, S., Coe, H., Cornet, C., Coutris, P., Couvreux, F., Crewell, S., Cronin, T., Cui, Z., Cuypers, Y., Daley, A., Damerell, G. M., Dauhut, T., Deneke, H., Desbios, J.-P., Dörner, S., Donner, S., Douet, V., Drushka, K., Dütsch, M., Ehrlich, A., Emanuel, K., Emmanouilidis, A., Etienne, J.-C., Etienne-Leblanc, S., Faure, G., Feingold, G., Ferrero, L., Fix, A., Flamant, C., Flatau, P. J., Foltz, G. R., Forster, L., Furtuna, I., Gadian, A., Galewsky, J., Gallagher, M., Gallimore, P., Gaston, C., Gentemann, C., Geyskens, N., Giez, A., Gollop, J., Gouirand, I., Gourbeyre, C., de Graaf, D., de Groot, G. E., Grosz, R., Güttler, J., Gutleben, M., Hall, K., Harris, G., Helfer, K. C., Henze, D., Herbert, C., Holanda, B., Ibanez-Landeta, A., Intrieri, J., Iyer, S., Julien, F., Kalesse, H., Kazil, J., Kellman, A., Kidane, A. T., Kirchner, U., Klingebiel, M., Körner, M., Kremper, L. A., Kretzschmar, J., Krüger, O., Kumala, W., Kurz, A., L'Hégaret, P., Labaste, M., Lachlan-Cope, T., Laing, A., Landschützer, P., Lang, T., Lange, D., Lange, I., Laplace, C., Lavik, G., Laxenaire, R., Le Bihan, C., Leandro, M., Lefevre, N., Lena, M., Lenschow, D., Li, Q., Lloyd, G., Los, S., Losi, N., Lovell, O., Luneau, C., Makuch, P., Malinowski, S., Manta, G., Marinou, E., Marsden, N., Masson, S., Maury, N., Mayer, B., Mayers-Als, M., Mazel, C., McGeary, W., McWilliams, J. C., Mech, M., Mehlmann, M., Meroni, A. N., Mieslinger, T., Minikin, A., Minnett, P., Möller, G., Morfa Avalos, Y., Muller, C., Musat, I., Napoli, A., Neuberger, A., Noisel, C., Noone, D., Nordsiek, F., Nowak, J. L., Oswald,

https://doi.org/10.5194/egusphere-2026-554
Preprint. Discussion started: 11 February 2026

L., Parker, D. J., Peck, C., Person, R., Philippi, M., Plueddemann, A., Pöhlker, C., Pörtge, V., Pöschl, U., Pologne, L., Posyniak, M., Prange, M., Quiñones Meléndez, E., Radtke, J., Ramage, K., Reimann, J., Renault, L., Reus, K., Reyes, A., Ribbe, J., Ringel, M., Ritschel, M., Rocha, C. B., Rochetin, N., Röttenbacher, J., Rollo, C., Royer, H., Sadoulet, P., Saffin, L., Sandiford, S., Sandu, I., Schäfer, M., Schemann, V., Schirmacher, I., Schlenczek, O., Schmidt, J., Schröder, M., Schwarzenboeck, A., Sealy, A., Senff, C. J., Serikov, I., Shohan, S., Siddle, E., Smirnov, A., Späth, F., Spooner, B., Stolla, M. K., Szkółka, W., de Szoeke, S. P., Tarot, S., Tetoni, E., Thompson, E., Thomson, J., Tomassini, L., Totems, J., Ubele, A. A., Villiger, L., von Arx, J., Wagner, T., Walther, A., Webber, B., Wendisch, M., Whitehall, S., Wiltshire, A., Wing, A. A., Wirth, M., Wiskandt, J., Wolf, K., Worbes, L., Wright, E., Wulfmeyer, V., Young, S., Zhang, C., Zhang, D., Ziemen, F., Zinner, T., and Zöger, M.: EUREC^{4}A, Earth System Science Data, 13, 4067–4119, https://doi.org/10.5194/essd-13-4067-2021, publisher: Copernicus GmbH, 2021.

Stull, R. B., ed.: An Introduction to Boundary Layer Meteorology, Springer Netherlands, Dordrecht, https://doi.org/10.1007/978-94-009-3027-8, 1988.

Terpstra, A., Renfrew, I. A., and Sergeev, D. E.: Characteristics of Cold-Air Outbreak Events and Associated Polar Mesoscale Cyclogenesis over the North Atlantic Region, Journal of Climate, 34, 4567–4584, https://doi.org/10.1175/JCLI-D-20-0595.1, 2021.

Tomassini, L., Field, P. R., Honnert, R., Malardel, S., McTaggart-Cowan, R., Saitou, K., Noda, A. T., and Seifert, A.: The "Grey Zone" cold air outbreak global model intercomparison: A cross evaluation using large-eddy simulations, Journal of Advances in Modeling Earth Systems, 9, 39–64, https://doi.org/10.1002/2016MS000822, _eprint: https://agupubs.onlinelibrary.wiley.com/doi/pdf/10.1002/2016MS000822, 2017.

Tornow, F., Ackerman, A. S., and Fridlind, A. M.: Preconditioning of overcast-to-broken cloud transitions by riming in marine cold air outbreaks, Atmospheric Chemistry and Physics, 21, 12 049–12 067, https://doi.org/10.5194/acp-21-12049-2021, publisher: Copernicus GmbH, 2021.

Tornow, F., Ackerman, A. S., Fridlind, A. M., Tselioudis, G., Cairns, B., Painemal, D., and Elsaesser, G.: On the Impact of a Dry Intrusion Driving Cloud-Regime Transitions in a Midlatitude Cold-Air Outbreak, Journal of the Atmospheric Sciences, 80, 2881–2896, https://doi.org/10.1175/JAS-D-23-0040.1, 2023.

Troen, I. B. and Mahrt, L.: A simple model of the atmospheric boundary layer; sensitivity to surface evaporation, Boundary-Layer Meteorology, 37, 129–148, https://doi.org/10.1007/BF00122760, 1986.

Vaisala: NCAR Dropsonde NRD41, B212680EN-A © Vaisala 2023, https://docs.vaisala.com/api/khub/documents/xFqIJ3AzmQb3A1csocKwLQ/content?Ft-Calling-App=ft%2Fturnkey-portal&Ft-Calling-App-Version=5.1.57#, 2023.

van der Dussen, J. J., de Roode, S. R., Ackerman, A. S., Blossey, P. N., Bretherton, C. S., Kurowski, M. J., Lock, A. P., Neggers, R. a. J., Sandu, I., and Siebesma, A. P.: The GASS/EUCLIPSE model intercomparison of the stratocumulus transition as observed during ASTEX: LES results, Journal of Advances in Modeling Earth Systems, 5, 483–499, https://doi.org/10.1002/jame.20033, _eprint: https://agupubs.onlinelibrary.wiley.com/doi/pdf/10.1002/jame.20033, 2013.

Voss, P. B., Zaveri, R. A., Flocke, F. M., Mao, H., Hartley, T. P., DeAmicis, P., Deonandan, I., Contreras-Jiménez, G., Martínez-Antonio, O., Figueroa Estrada, M., Greenberg, D., Campos, T. L., Weinheimer, A. J., Knapp, D. J., Montzka, D. D., Crounse, J. D., Wennberg, P. O., Apel, E., Madronich, S., and de Foy, B.: Long-range pollution transport during the MILAGRO-2006 campaign: a case study of a major Mexico City outflow event using free-floating altitude-controlled balloons, Atmospheric Chemistry and Physics, 10, 7137–7159, https://doi.org/10.5194/acp-10-7137-2010, 2010.

Walbröl, A., Michaelis, J., Becker, S., Dorff, H., Ebell, K., Gorodetskaya, I., Heinold, B., Kirbus, B., Lauer, M., Maherndl, N., Maturilli, M., Mayer, J., Müller, H., Neggers, R. A. J., Paulus, F. M., Röttenbacher, J., Rückert, J., Schirmacher, I., Slättberg, N., Ehrlich, A.,

https://doi.org/10.5194/egusphere-2026-554
Preprint. Discussion started: 11 February 2026

Wendisch, M., and Crewell, S.: Contrasting extremely warm and long-lasting cold air anomalies in the North Atlantic sector of the Arctic during the HALO-$(AC)^3$ campaign, Atmospheric Chemistry and Physics, https://doi.org/10.5194/acp-24-8007-2024, 2024.

Wang, J. J., Young, K., Hock, T., Lauritsen, D., Behringer, D., Black, M., Black, P. G., Franklin, J., Halverson, J., Molinari, J., Nguyen, L., Reale, T., Smith, J., Sun, B., Wang, Q., and Zhang, J. A.: A Long-Term, High-Quality, High-Vertical-Resolution GPS Dropsonde Dataset for Hurricane and Other Studies, Bulletin of the American Meteorological Society, https://doi.org/10.1175/BAMS-D-13-00203.1, section: Bulletin of the American Meteorological Society, 2015.

Wendisch, M., Crewell, S., Ehrlich, A., Herber, A., Kirbus, B., Lüpkes, C., Mech, M., Abel, S. J., Akansu, E. F., Ament, F., Aubry, C., Becker, S., Borrmann, S., Bozem, H., Brückner, M., Clemen, H.-C., Dahlke, S., Dekoutsidis, G., Delanoë, J., De La Torre Castro, E., Dorff, H., Dupuy, R., Eppers, O., Ewald, F., George, G., Gorodetskaya, I. V., Grawe, S., Groß, S., Hartmann, J., Henning, S., Hirsch, L., Jäkel, E., Joppe, P., Jourdan, O., Jurányi, Z., Karalis, M., Kellermann, M., Klingebiel, M., Lonardi, M., Lucke, J., Luebke, A. E., Maahn, M., Maherndl, N., Maturilli, M., Mayer, B., Mayer, J., Mertes, S., Michaelis, J., Michalkov, M., Mioche, G., Moser, M., Müller, H., Neggers, R., Ori, D., Paul, D., Paulus, F. M., Pilz, C., Pithan, F., Pöhlker, M., Pörtge, V., Ringel, M., Risse, N., Roberts, G. C., Rosenburg, S., Röttenbacher, J., Rückert, J., Schäfer, M., Schaefer, J., Schemann, V., Schirmacher, I., Schmidt, J., Schmidt, S., Schneider, J., Schnitt, S., Schwarz, A., Siebert, H., Sodemann, H., Sperzel, T., Spreen, G., Stevens, B., Stratmann, F., Svensson, G., Tatzelt, C., Tuch, T., Vihma, T., Voigt, C., Volkmer, L., Walbröl, A., Weber, A., Wehner, B., Wetzel, B., Wirth, M., and Zinner, T.: Overview: quasi-Lagrangian observations of Arctic air mass transformations – introduction and initial results of the HALO–$(AC)^3$ aircraft campaign, Atmospheric Chemistry and Physics, 24, 8865–8892, https://doi.org/10.5194/acp-24-8865-2024, publisher: Copernicus GmbH, 2024.

Wendisch, M., Kirbus, B., Ori, D., Shupe, M. D., Crewell, S., Sodemann, H., and Schemann, V.: Observed and modeled Arctic air-mass transformations during warm air intrusions and cold air outbreaks, Atmospheric Chemistry and Physics, 25, 15 047–15 076, https://doi.org/10.5194/acp-25-15047-2025, 2025.

Wu, P., Ovchinnikov, M., Xiao, H., Lackner, C. P., Geerts, B., Tornow, F., and Elsaesser, G.: Effect of Ice Number Concentration on the Evolution of Boundary Layer Clouds During Arctic Marine Cold-Air Outbreaks, Journal of Geophysical Research: Atmospheres, 130, e2024JD041 282, https://doi.org/10.1029/2024JD041282, _eprint: https://agupubs.onlinelibrary.wiley.com/doi/pdf/10.1029/2024JD041282, 2025.

Young, G., Connolly, P. J., Dearden, C., and Choularton, T. W.: Relating large-scale subsidence to convection development in Arctic mixed-phase marine stratocumulus, Atmospheric Chemistry and Physics, 18, 1475–1494, https://doi.org/10.5194/acp-18-1475-2018, publisher: Copernicus GmbH, 2018.

Zhou, X., Kollias, P., and Lewis, E. R.: Clouds, Precipitation, and Marine Boundary Layer Structure during the MAGIC Field Campaign, Journal of Climate, 28, 2420–2442, https://doi.org/10.1175/JCLI-D-14-00320.1, 2015.